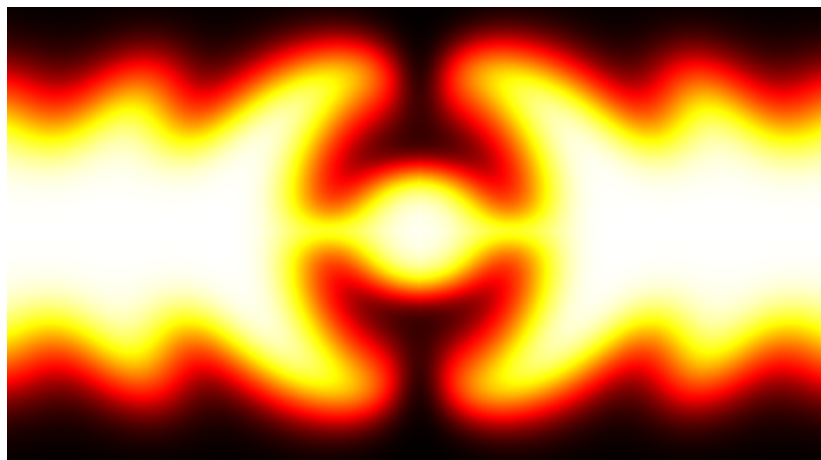


Master Thesis

# Theory and modeling of acoustofluidics with inhomogeneous solutions

Gustav K. Modler  
s173728



Supervisor: Henrik Bruus

Department of Physics  
Technical University of Denmark

15 July 2023



# Abstract

Acoustofluidics combines microscale acoustics and fluid dynamics to facilitate precise and gentle manipulation of biological cells using acoustic radiation forces. The field encompasses a wide range of applications, including devices for particle focusing and separation, as well as traps and tweezers for selective particle manipulation. However, effectively manipulating small microparticles with sizes below 1 micrometer poses challenges due to the interplay of multiple competing forces. Nevertheless, the recent discovery of the acoustic force density has opened up new possibilities for manipulating fluids and suspended particles, necessitating further investigation and exploration of this force.

The acoustic force density emerges on inhomogeneous solutions of miscible fluids placed in acoustic fields. The force density arises due to interactions between the acoustic fields and the gradients in density and compressibility of the inhomogeneous solutions. The force density compels the solutions to move into spatiotemporally controllable configurations, which subsequently dissolves by diffusion.

In this thesis, we theoretically investigate the patterning of inhomogeneous solutions of Ficoll PM400 with acoustic vortices in a shallow microfluidic chamber. This specific system is inspired by our experimental collaborators at University of Lille in the Institut d'électronique de microélectronique et de nanotechnologie (IEMN). Employing both height-averaged 2D models and a 3D model, simulations of the system are carried out to determine the significant processes involved in the patterning when the system is geometrically confined between two narrowly spaced parallel plates. Notably, the shearing caused by the top and bottom walls resulted in significant viscous resistance and enhanced diffusion by classical Taylor dispersion. The final 2D model tested favorably against the 3D model, but fell short in accurately describing the diffusive dissolution of the pattern when compared with experimental data.



# Resumé

Akustofluidik kombinerer mikroskalaakustik og væskedynamik for at udføre præcis og skånsom manipulation af biologiske celler ved hjælp af akustiske strålingskræfter. Feltet omfatter en bred vifte af anvendelser, herunder miniaturiserede apparater til partikelfokusering og -separation, samt fælder og pincetter til selektiv partikelmanipulation. Effektiv manipulation af små mikropartikler med størrelser under 1 mikrometer udgør dog udfordringer på grund af samspillet mellem flere konkurrerende kræfter. Ikke desto mindre har den nylige opdagelse af den akustiske krafttæthed åbnet nye muligheder for at manipulere væsker og suspenderede partikler, hvilket nødvendiggør yderligere undersøgelse og udforskning af denne kraft.

Den akustiske krafttæthed opstår på inhomogene opløsninger af blandbare væsker placeret i akustiske felter. Krafttætheden opstår på grund af vekselvirkninger mellem de akustiske felter og gradienterne i massetæthed og kompressibilitet af de inhomogene opløsninger. Den tvinger opløsningerne til at bevæge sig ind i rumligt og tidsmæssigt kontrollerbare konfigurationer, som derefter opløses ved diffusion.

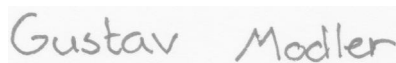
I dette speciale undersøges teoretisk mønsterdannelsen af Ficoll PM400 med en akustisk pincet i et snævert mikrokammer. Dette system er inspireret af vores eksperimentelle samarbejdspartnere ved Lille Universitet i IEMN laboratoriet. Ved at anvende både 2D-modeller med højdegnemsnit samt en 3D model, udføres simuleringer af systemet for at kortlægge de væsentlige processer, der er involveret i dannelsen af mønsteret, når systemet er geometrisk afgrænset mellem to snævert adskilte parallelle plader. Den endelige 2D-model testede positivt mod 3D-modellen, men kom til kort med at beskrive den diffusive opløsning af mønsteret nøjagtigt sammenlignet med eksperimentelle data.



# Preface

This master's thesis is submitted in partial fulfilment of obtaining the degree of Master of Science in Engineering Physics at the Technical University of Denmark (DTU). This thesis corresponds to 32.5 ECTS points, and the work was carried out from February 2023 to July 2023 at DTU Physics in the Theoretical Microfluidics Group (TMF) headed by Prof. Henrik Bruus.

I would like to express my gratitude to Professor Henrik Bruus for his support and guidance throughout my master's degree and this thesis. I also want to extend my thanks to the current and past members of TMF: Søren Kuhberg, Bjørn Winckelmann, William Naundrup Bodé, and Fabian Lickert, for the scientific discussions and the camaraderie. This also goes out to my colleagues within the wider Biophysics and Fluids section: Matt Dominic Biviano, Peter Bork, Anneline Hegelund Christensen, Sabrina Gennis, John Sebastian, Sif Fink Arnbjerg-Nielsen, and Magnus Valdemar Paludan. Furthermore, I want to extend my gratitude to my friend Melissa Mai of Harvard University, for her remarkable inspiration, support, and encouragement throughout this thesis. I also want to express my appreciation to our experimental collaborators, PhD student Samir Almohamad, Chargé de recherche Sarah Cleve, and Professor Michaël Baudoin, from Lille University, for our collaboration, discussions and their invaluable input. Finally, I want to thank Jonathan of my dorm, for reading through the thesis and providing feedback.



Gustav Kildevang Modler  
Department of Physics  
Technical University of Denmark  
15 July 2023



# Contents

List of figures	xii
List of tables	xiii
List of symbols	xv
<b>1 Introduction</b>	<b>1</b>
1.1 Acoustofluidics	1
1.2 Motivation and goal	2
<b>2 Theoretical framework</b>	<b>5</b>
2.1 The continuum description of fluids	5
2.2 Fluid dynamics	5
2.3 Mass transport in inhomogeneous solutions	7
2.4 Acoustofluidics of inhomogeneous solutions	8
<b>3 Numerical simulations with COMSOL Multiphysics</b>	<b>11</b>
3.1 Finite element method	11
3.1.1 Discretization	12
3.1.2 The weak formulation of a PDE	12
3.1.3 Boundary conditions on weak form	13
3.1.4 Symmetry conditions	14
3.2 Numerical stability and mesh refinement study	14
3.2.1 Stability criteria	14
3.2.2 Probes	15
3.2.3 Mesh refinement study	16
<b>4 The 3D model</b>	<b>19</b>
4.1 Formulation of 3D model	19

4.2	Model implementation . . . . .	25
4.3	Results and discussion . . . . .	27
<b>5</b>	<b>The 2D Hele-Shaw model</b>	<b>31</b>
5.1	Long-wavelength formulation . . . . .	31
5.1.1	Non-dimensionalization of governing equations . . . . .	32
5.1.2	Derivation of height-averaged equations . . . . .	33
5.2	Results and discussion . . . . .	36
5.3	Dispersion . . . . .	40
5.3.1	Dispersion model . . . . .	40
5.3.2	Results and discussion . . . . .	42
<b>6</b>	<b>The improved 2D Hele-Shaw model</b>	<b>47</b>
6.1	Improved 2D model formulation . . . . .	47
6.2	Results and discussion of contrast curves . . . . .	48
6.3	Exploring parameter space . . . . .	49
<b>7</b>	<b>Experimental comparisons</b>	<b>55</b>
7.1	Determining the initial concentration profile . . . . .	55
7.2	Comparison of simulations and experimental data . . . . .	56
<b>8</b>	<b>Conclusion &amp; Outlook</b>	<b>59</b>
<b>A</b>	<b>Instantaneous point-source diffusion in cylindrical box</b>	<b>61</b>
<b>B</b>	<b>Gravity simulation</b>	<b>65</b>
<b>C</b>	<b>Acoustics and gravity</b>	<b>67</b>
<b>D</b>	<b>Influence of viscosity variation</b>	<b>69</b>
	<b>Bibliography</b>	<b>69</b>

# List of Figures

1.1	Patterning using acoustic tweezers . . . . .	3
2.1	Plot of $s$ -dependencies of parameters . . . . .	8
3.1	Triangular mesh . . . . .	12
3.2	Results of probes . . . . .	15
3.3	Mesh convergence plot . . . . .	17
4.1	Sketch of microfluidic chamber . . . . .	19
4.2	Initial solute concentration profile . . . . .	20
4.3	Acoustic pressure field and force-shape function . . . . .	22
4.4	Sketch of geometry . . . . .	25
4.5	Patterning of Ficoll PM400 . . . . .	28
4.6	Acoustic-induced flow field . . . . .	30
5.1	Height-profile of velocity . . . . .	37
5.2	Contrast curve of 2D Hele-Shaw model . . . . .	38
5.3	Comparison of 2D Hele-Shaw models with and without dispersion . . . . .	43
5.4	Influence of dispersion . . . . .	44
6.1	Comparison of contrast curves of improved 2D model . . . . .	48
6.2	Sweep on maximum normal displacement . . . . .	50
6.3	Sweep on maximum concentration value . . . . .	52
6.4	Sweeps on initial width and gradient width of Ficoll-band . . . . .	54
7.1	Experimental data of initial Ficoll concentration profile . . . . .	56
7.2	Comparison of concentration contrast of simulation and experiment . . . . .	57
7.3	Comparison of pattern of simulation and experiment . . . . .	58

A.1	Sketch of cylindrical box . . . . .	62
A.2	Diffusion in cylindrical box . . . . .	63
B.1	Sketch of microfluidic chamber . . . . .	65
B.2	Relative concentration variation due to convection . . . . .	66
C.1	Influence of gravity with acoustics . . . . .	67
D.1	Influence of variation of viscosity over height . . . . .	70

# List of Tables

2.1	Parameter values of Ficoll PM400 . . . . .	8
4.1	Default parameter values in simulations . . . . .	25
7.1	Parameter values for experimental comparison . . . . .	57



# Symbols

Symbol	Description	Unit
$\rho$	Mass density	$\text{kg m}^{-3}$
$p$	Pressure	Pa
$s$	Concentration	1
$\mathbf{v}$	Fluid velocity	$\text{m s}^{-1}$
$\boldsymbol{\sigma}$	Stresses	Pa
$\mathbf{f}$	Body force densities	$\text{N m}^{-3}$
$\eta$	Shear viscosity	Pa s
$\eta^b$	Bulk viscosity	Pa s
$\kappa$	Compressibility	$\text{m}^2 \text{N}^{-1}$
$c$	Sound speed	$\text{m s}^{-1}$
$c_g$	Transverse sound speed in glass	$\text{m s}^{-1}$
$D$	Diffusivity	$\text{m}^2 \text{s}^{-1}$
$U_0$	Characteristic flow speed	$\text{m s}^{-1}$
$L_0$	Characteristic length	m
$h_{\text{mesh}}$	Mesh element size	m
$\tau_{\text{adv}}$	Advective time scale	s
$\tau_{\text{diff}}$	Diffusive time scale	s
$\tau_{\text{diff}}^{\parallel}$	Long diffusive time scale	s
$\tau_{\text{hyd}}$	Hydrodynamic time scale	s
$\tau_{\text{ac}}$	Acoustic time scale	s
$\epsilon$	Acoustic aspect ratio	1
$Re$	Reynolds number	1
$Pe$	Péclet number	1
$Pe_{\text{cell}}$	Cell Péclet number	1
$Co$	Courant number	1
$\mathcal{D}$	Discrepancy	1

$L$	Length	m
$W$	Width	m
$h$	Height	m
$f$	Frequency	$s^{-1}$
$\omega$	Angular frequency	$\text{rad s}^{-1}$
$\lambda$	Wavelength	m
$k$	Wave number	$\text{m}^{-1}$
$p_{\text{ac}}^{\text{max}}$	Acoustic pressure maximum	Pa
$d_{\text{n}}^{\text{max}}$	Maximum normal displacement	m
$s_{\text{min}}$	Minimum initial solute concentration	1
$s_{\text{max}}$	Maximum initial solute concentration	1
$C$	Concentration contrast	1
$y_0$	Initial concentration width	m
$w_0$	Initial concentration gradient width	m
$\zeta$	Velocity height-profile	1
$\partial_t$	Explicit time derivative	$s^{-1}$
$\partial_i$	Derivative in $i$ with $i = x, y, z$	$\text{m}^{-1}$
$\nabla$	Gradient	$\text{m}^{-1}$
$d_t$	Material derivative	$s^{-1}$
$\nabla \cdot$	Divergence	$\text{m}^{-1}$
$\nabla \times$	Curl	$\text{m}^{-1}$
$\nabla_{\parallel}$	Gradient in $x$ - and $y$ -coordinates	$\text{m}^{-1}$

# Chapter 1

## Introduction

### 1.1 Acoustofluidics

Acoustofluidics is the synthesis of acoustics and microfluidics. The field has emerged at the interface of physics, engineering, and biology as a promising field, enabling novel technologies and revolutionizing existing ones within lab-on-a-chip systems and biomedical applications such as point-of-care diagnostics. Utilizing ultrasonic waves to precisely control and manipulate fluids and particles at the microscale, acoustofluidic technology offers unique capabilities for analysis and isolation of bio-particles in a contact-free and bio-compatible manner, making it desirable for biomedical applications [1].

Fundamentally, acoustofluidic technology relies on acoustic radiation forces that are exerted upon particles by acoustic waves. These forces arise from the scattering of the waves with the particles, resulting in the transfer of momentum from the waves to the particles [2, 3, 4, 5]. Summarized in the acoustic contrast factors of particles, the relative compressibilities and densities of the particles to those of the fluid medium decide the directions of the forces. These contrast factors are exploited in acoustophoretic devices to focus, separate, and trap particles [6, 7].

The acoustic radiation forces on particles scales with the particles' volumes, whereas the Stokes drag forces from impinging fluid flows scale with their radii. These different scalings lead to critical radii on the order of  $1\ \mu\text{m}$ , below which the motions of particles are dominated by drag forces from acoustic microstreaming [8, 9]. This microstreaming, also known as Rayleigh streaming or boundary-driven streaming, is a steady circulating flow that arises from viscous dissipation of acoustic waves within thin boundary layers at solid surfaces [10] and is generally undesirable.

More recently, standing acoustic waves have been discovered to stabilize inhomogeneous fluid solutions against gravity [11]. This discovery led to the subsequent development of iso-acoustic focusing of cells technique for size-insensitive acousto-mechanical phenotyping [12]. Karlsen and Bruus provided the theoretical explanation of the phenomenon, attributing it to time-averaged acoustic force densities that arise in fluids exhibiting continuous spatial variations in their densities and compressibilities; the variations produce a non-zero divergence of the time-averaged momentum-flux density, which is absent in

immiscible fluids, lacking the continuous spatial variations [13]. The focus of my thesis revolves around this acoustic force density.

## 1.2 Motivation and goal

Shortly after their findings, Karlsen and Bruus theoretically demonstrated the application of acoustic vortices to pattern and manipulate solute concentration fields into spatiotemporally controllable configurations that could be translated within the medium, using the acoustic force density [15]. Our experimental collaborators PhD student Samir Almohamad, CR Sarah Cleve, and Professor Michaël Baudoin at Lille University provided the experimental evidence for this patterning using a Ficoll solution in water and an acoustic tweezer [14]. The same acoustic tweezer is used to selectively trap and manipulate 10  $\mu\text{m}$ -size biological cells, demonstrated by Baudoin et al., using the focalized acoustic vortices to create the tightly focused trap necessary for achieving this [7].

This tweezer-setup consisting of a shallow microfluidic chamber, a glass substrate, and the tweezer itself is shown in Fig. 1.1(a) adapted from Ref. [7]. Inside the chamber, a band of Ficoll PM400 (dark fluid) positioned along the longitudinal axis of the chamber is inserted with Milli-Q water (light fluid) on either side by its introduction via an inlet, squeezed between two streams of the water. The subsequent patterning of the solution is shown in Fig. 1.1(b) adapted from Ref. [14]. Initially, the two fluids are at rest (A). Upon activation of the acoustic tweezer, protrusions occur at the interface of the fluids (B–D), leading to the formation of a pattern (E), which dissolves by diffusion (F). They quantified the sharpness of the pattern by the difference between the concentration of Ficoll at the center of the vortex and an averaged concentration on the circle coinciding with the first clearance of Ficoll, with center at the vortex. This defines the concentration contrast  $C$  that has been plotted vs. time  $t$  in Fig. 1.1(c). A characteristic time of patterning  $t^*$  can be defined as the time at which  $C$  attains its maximum value,  $C_{\text{max}}$ .

Ultimately, the goal of investigating this manipulation of inhomogeneous solutions is to develop a device that can aggregate small bio-particles. Similar to the iso-acoustic focusing technique, this device is based on the gradient in acoustic impedance created by the inhomogeneous solution. In this gradient, the bio-particles are trapped at their particle-type specific point of zero acoustic contrast. The acoustic tweezer localizes the gradient to a small region surrounding the acoustic center, which can be moved to the small bio-particles. To this end, this thesis aims to develop a numerical model that describes the patterning of the Ficoll solution observed inside the shallow microfluidic chamber. The thesis thus expands upon the theory of Karlsen and Bruus by extending the analysis to a 3D system.

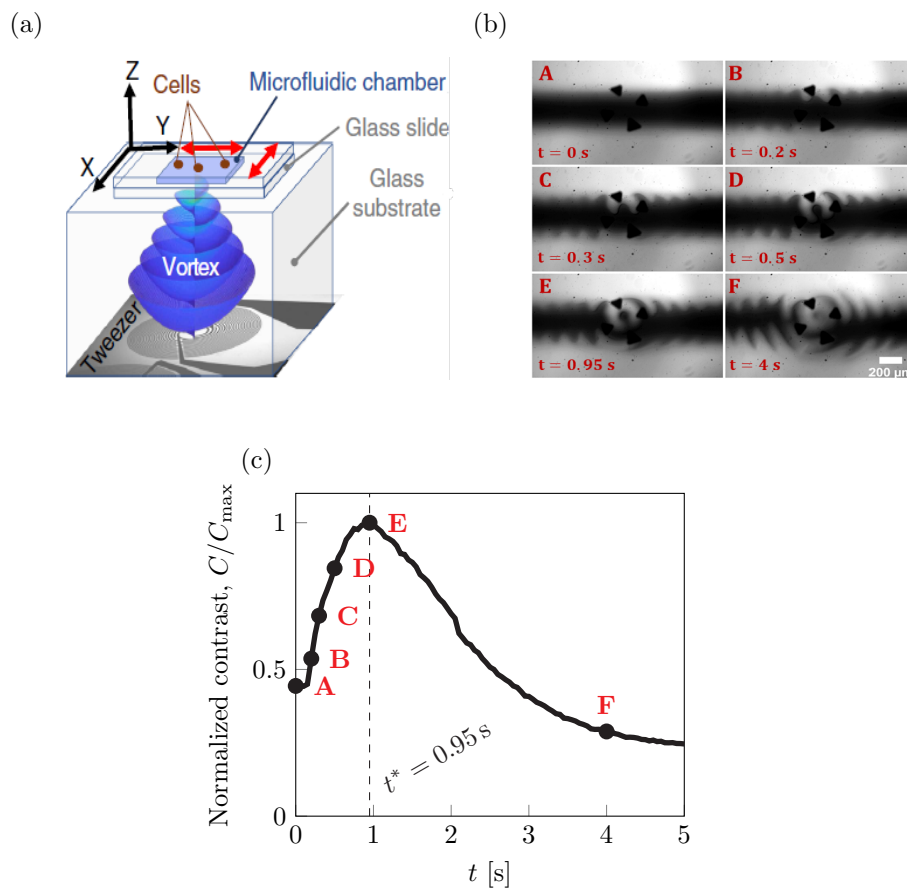


Figure 1.1: Patterning of Ficoll PM400 in water using acoustic tweezers. (a) Sketch of acoustic tweezer setup used for trapping  $10 \mu\text{m}$ -size bio-particles. The setup comprises an acoustic tweezer, which produces the acoustic vortices that propagate and focalize inside a glass substrate before hitting a shallow microfluidic chamber containing the cells. Adapted from Ref. [7]. (b) Patterning of Ficoll PM400 (dark fluid) in Milli-Q water (light fluid) using the setup in (a). Each panel depicts a different time during the evolution of the pattern. Adapted from Ref. [14]. (c) The concentration contrast defined as the difference between concentration at acoustic center and averaged along first node of concentration field. Panels A–F are indicated on the curve. Reproduced from Ref. [14]. Courtesy of Almohamad providing the data.



## Chapter 2

# Theoretical framework

To describe the patterning of inhomogeneous solutions induced by acoustic fields, we need equations that describe the dynamic behaviour of fluids under external forcing. In this chapter, these governing equations are introduced in Secs. 2.2 and 2.3 and subsequently applied in Sec. 2.4 to derive the theory of acoustofluidics of inhomogeneous solutions, including the aforementioned acoustic force density formulated originally by Karlsen and Bruus [13]. For more detailed expositions of the basic equations, see Refs. [16, 17, 18, 19].

### 2.1 The continuum description of fluids

The theory of fluid mechanics is formulated with the concept of a volume element. The volume element represents a small volume within the much larger fluid medium. This volume is sufficiently small to exhibit uniform properties, including pressure, density, velocity, temperature, etc., whose values are defined by their statistical averages over the molecules contained within the volume. Therefore, this volume also need to be large enough to eliminate statistical fluctuations by encompassing a significant number of molecules. In this framework, each point in space is associated with a volume element, so by considering all volume elements distributed throughout the fluid medium, the immediate state of the fluid can be described by these properties as functions of space and time referred to as ‘fields’. The governing equations of its evolution are then obtained on local form by applying the classical conservation laws to a volume element.

### 2.2 Fluid dynamics

The governing equations for fluid flows are the continuity equation and the Navier–Stokes equations, expressing the conservation of mass and the conservation of momentum, respectively. In terms of the local fluid density  $\rho$ , the local flow velocity  $\mathbf{v}$ , the local stresses  $\boldsymbol{\sigma}$ , and the local force densities  $\mathbf{f}$ , the

equations can be written as

$$\partial_t \rho + (\mathbf{v} \cdot \nabla) \rho = -\rho \nabla \cdot \mathbf{v}, \quad (2.1a)$$

$$\rho \partial_t \mathbf{v} + \rho (\mathbf{v} \cdot \nabla) \mathbf{v} = \nabla \cdot \boldsymbol{\sigma} + \mathbf{f}, \quad (2.1b)$$

in which  $\partial_t$  represents the time rate of change, and  $\mathbf{v} \cdot \nabla$  the advective rate of change arising from the relocation of the fluid itself. The operator defined as

$$d_t \equiv \partial_t + (\mathbf{v} \cdot \nabla) \quad (2.2)$$

combines both rates of change and describes the rate of change experienced by a fluid particle as it moves through the flow field.

The continuity equation (2.1a) relates this co-moving rate of change of density to a net outflow rate of fluid volume  $\nabla \cdot \mathbf{v}$ . In the case of incompressible flow, in which the density remains constant everywhere in the fluid, this outflow rate must therefore vanish,

$$\nabla \cdot \mathbf{v} = 0. \quad (2.3)$$

This result, valid for flows in which the flow speeds are much smaller than the speed of sound, constitutes a major simplification of the equations, because it eliminates  $\rho$  as a variable.

Similarly, the Navier–Stokes equations (2.1b) relates the co-moving rate of change of velocity, i.e., the acceleration, multiplied by  $\rho$  to the momentum entering or leaving the volume through stresses exerted on its surfaces and forces acting throughout the volume. The stresses consists of a pressure  $p$  and viscous stresses  $\boldsymbol{\tau}$ . Given a Newtonian fluid,  $\boldsymbol{\tau}$  is directly proportional to the local rates of strain,  $\nabla \mathbf{v}$  and  $(\nabla \mathbf{v})^T$ , and the stresses  $\boldsymbol{\sigma}$  are given by

$$\boldsymbol{\sigma} = -p \mathbf{I} + \boldsymbol{\tau}, \quad \boldsymbol{\tau} = \eta [\nabla \mathbf{v} + (\nabla \mathbf{v})^T] + (\eta^b - \frac{2}{3} \eta) (\nabla \cdot \mathbf{v}) \mathbf{I}, \quad (2.4)$$

in which  $\mathbf{I}$  is the unit tensor, and  $\eta$  and  $\eta^b$  are the shear and bulk viscosities, respectively.

The viscous stresses introduce a flow resistance that is particularly pronounced on the micro-scale or in close proximity of solid surfaces, where the fluid velocity must match that of the boundary expressed by the no-slip condition:

$$\mathbf{v} = \mathbf{0}, \quad (2.5)$$

for the relative velocity.

The Reynolds number  $Re$  is defined as the ratio of inertial forces to that of viscosity. If  $U_0$  is the characteristic flow speed and  $L_0$  the characteristic length, it is given by

$$Re = \frac{\rho U_0 L_0}{\eta}. \quad (2.6)$$

For very small Reynolds numbers,  $Re \ll 1$ , viscosity is the dominant factor, and the flow is laminar. In this

regime, the non-linear advective term in the Navier–Stokes equations (2.1b) is negligible, which greatly simplifies the equations. Furthermore, if the relevant time scale is  $L_0/U_0$ , the explicit time-dependency of the velocity can also be disregarded. In microfluidic systems, where flow velocities typically are on the order of  $0.1 \text{ mm s}^{-1}$  and length scales around  $100 \text{ }\mu\text{m}$ , the Reynolds number is  $Re \sim 0.01 \ll 1$ , using  $\eta \sim 1 \text{ mPa}\cdot\text{s}$  and  $\rho \sim 1000 \text{ kg m}^{-3}$ .

## 2.3 Mass transport in inhomogeneous solutions

We consider an inhomogeneous fluid solution of Ficoll PM400 dissolved in water. Introducing the local solute concentration  $s$  in mass ratio to represent the Ficoll solution, the total density of this solution is given by

$$\rho = \rho_w(1 + a_1 s), \quad (2.7)$$

with  $\rho_w$  being the density of the solvent—the water—and  $a_1 \equiv (1/\rho_w)(\partial\rho/\partial s)_T$  the relative change of density to solvent density per change in solute concentration.

The equations of the preceding section still apply to this heterogeneous solution of Ficoll and water. However, with the introduction of  $s$ , we need to include the convection-diffusion equation to take into account the mass conservation of the Ficoll solution. This equation is given by

$$\partial_t s + (\mathbf{v} \cdot \nabla)s = \nabla \cdot (D \nabla s), \quad (2.8)$$

in which  $D$  is the diffusivity, representing the rate of diffusive spread of Ficoll in water. Like the total density, this diffusivity, the viscosity, and the speed of sound in the solution depend on the local concentration of the Ficoll solution. Summarized, the concentration-dependencies of the parameters of the solution have experimentally been determined to be [20]

$$\begin{aligned} \rho &= \rho_w(1 + a_1 s), & \eta &= \eta_w \exp(bs), & c &= c_w(1 + c_1 s), \\ D &= D_w(1 + d_1 s + d_2 s^2). \end{aligned} \quad (2.9)$$

in which  $\rho_w$ ,  $\eta_w$ ,  $c_w$ ,  $D_w$ ,  $a_1$ ,  $b$ ,  $c_1$ ,  $d_1$ , and  $d_2$  are constants, whose values have been tabulated in Tab. 2.1. The parameters have been plotted against  $s$  in Fig. 2.1.

At impenetrable boundaries, such as solid walls, there can be no mass transport across the boundary. This condition of zero mass-flux is expressed by the following boundary condition at solid boundaries:

$$(\hat{\mathbf{n}} \cdot \nabla)s = 0, \quad (2.10)$$

with  $\hat{\mathbf{n}} \cdot \nabla$  denoting the derivative taken with respect to the normal direction of the boundary.

The ratio of advective transport to diffusive spreading is known as the Péclet number  $Pe$ . In terms of the characteristic quantities  $U_0$  and  $L_0$  and the diffusivity  $D$ , this dimensionless number is given by

$$Pe = \frac{U_0 L_0}{D}. \quad (2.11)$$

Table 2.1: Values of the parameters entering Eq. (2.9) expressing the concentration-dependencies of the density, viscosity, sound speed, and diffusivity of Ficoll PM400 in Milli-Q water at 25 °C [20].

<i>Pure Milli-Q water</i>			<i>Derivatives</i>		
Symbol	Value	Units	Symbol	Value	Units
$\rho_w$	996.91	$\text{kg m}^{-3}$	$a_1$	0.348	1
$\eta_w$	0.893	$\text{mPa s}$	$b$	16.2	1
$c_w$	1496.5	$\text{m s}^{-1}$	$c_1$	0.164	1
$D_w$	$1.15 \times 10^{-10}$	$\text{m}^2 \text{s}^{-1}$	$d_1$	-10.3	1
			$d_2$	56.0	1

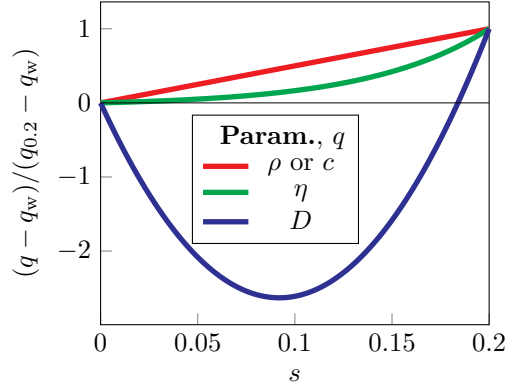


Figure 2.1: Plot of the parameters  $\rho$ ,  $\eta$ ,  $c$ , and  $D$ , collectively denoted by  $q$ , vs. the Ficoll concentration  $s$  expressed by mass ratio. It shows the difference  $q(s) - q_w$  from the pure-water value  $q_w$ , normalized by  $q(0.2) - q_w$ .

For very small values of  $Pe$ , the transport is primarily governed by diffusion. Conversely, in the opposite limit in which  $Pe$  becomes very large, advection is the dominant transport mechanism.

## 2.4 Acoustofluidics of inhomogeneous solutions

The flows of inhomogeneous solutions of miscible fluids in acoustic fields are driven by the acoustic force density denoted  $\mathbf{f}_{\text{ac}}$ . The flow occurs on the hydrodynamic time scale  $\tau_{\text{hyd}} = 1/kU_0$ , with  $k = \omega/c$  being the wave number of the acoustics and  $\omega$  the angular frequency. This time scale is slow compared to the acoustic time scale,  $\tau_{\text{ac}} = 1/\omega$ , leading to  $\tau_{\text{ac}}/\tau_{\text{hyd}} = (1/\omega)/(1/kU_0) = U_0/c \ll 1$ . Accordingly, the acoustic fields can be represented by first-order time-harmonic terms of a perturbation expansion around the zeroth-order state describing a quiescent fluid. Using the complex notation of harmonic oscillations,

the fields can be written as

$$\rho(\mathbf{r}, t) = \rho_0(\mathbf{r}, t) + \rho_1(\mathbf{r})e^{-i\omega t}, \quad (2.12a)$$

$$p(\mathbf{r}, t) = p_0(\mathbf{r}, t) + p_1(\mathbf{r})e^{-i\omega t}, \quad (2.12b)$$

$$\mathbf{v}(\mathbf{r}, t) = \mathbf{v}_1(\mathbf{r})e^{-i\omega t}, \quad (2.12c)$$

in which the zeroth-order state parameters  $\rho_0$  and  $p_0$  vary in space, although slowly. In this notation, the physical field corresponds to the real part of the complex field.

The acoustic density changes  $\rho_1$  and the acoustic pressure changes  $p_1$  can be related using the thermodynamic relation  $d\rho = c^{-2}dp$ , with  $c$  being the adiabatic sound speed. Because the fluid medium is inhomogeneous, this thermodynamic equation relates their material derivatives (2.2),

$$d_t\rho(\mathbf{r}, t) = c^{-2}d_t p(\mathbf{r}, t). \quad (2.13)$$

To first order, this relation leads to

$$-i\omega\rho_1 + (\mathbf{v}_1 \cdot \nabla)\rho_0 \approx c_0^{-2}(-i\omega p_1), \quad (2.14)$$

in which the term  $c_0^{-2}(\mathbf{v}_1 \cdot \nabla)p_0$  has been neglected on account of its smallness, and the zeroth-order (adiabatic) sound speed  $c_0$  is given by

$$c_0^{-2} = \left( \frac{\partial\rho_1}{\partial p_1} \right)_S = \rho_0\kappa_0, \quad (2.15)$$

with  $\kappa_0$  the zeroth-order compressibility.

The first-order equations are comprised of the continuity equation and linearized inviscid<sup>1</sup> Navier–Stokes equations. Upon application of Eq. (2.14), these equations are

$$-i\omega c_0^{-2}p_1 = -\rho_0\nabla \cdot \mathbf{v}_1, \quad (2.16a)$$

$$-i\omega\rho_0\mathbf{v}_1 = -\nabla p_1, \quad (2.16b)$$

which combines to give

$$k_0^2 p_1 = \rho_0 \nabla \cdot \left( \frac{1}{\rho_0} \nabla p_1 \right), \quad k_0 = \frac{\omega}{c_0}, \quad (2.17)$$

describing the propagation of acoustic pressure waves in inhomogeneous fluid media.

The acoustic force density derives from a nonzero divergence of the time-averaged (denoted  $\langle \cdot \rangle_t$ ) momentum flux-tensor  $\langle \mathbf{\Pi} \rangle_t$ ,

$$\mathbf{f}_{\text{ac}} = -\nabla \cdot \langle \mathbf{\Pi} \rangle_t \quad \text{with} \quad \langle \mathbf{\Pi} \rangle_t = \langle p_2 \rangle_t \mathbf{I} + \langle \rho_0 \mathbf{v}_1 \mathbf{v}_1 \rangle_t. \quad (2.18)$$

---

<sup>1</sup>For ultrasonic waves, the viscous damping factor is  $\sim 10^{-5} \ll 1$  in water, making it negligible far away from solid surfaces.

Here,  $\langle p_2 \rangle_t$  is the second-order mean Eulerian pressure given by

$$\langle p_2 \rangle_t = \frac{1}{4} \kappa_0 |p_1|^2 - \frac{1}{4} \rho_0 |v_1|^2, \quad (2.19)$$

which is obtained by integration of the time-averaged second-order inviscid Navier–Stokes equation. On substituting for  $\langle p_2 \rangle_t$  in Eq. (2.18) from the foregoing and applying the divergence, the acoustic force density is evaluated as

$$\mathbf{f}_{\text{ac}} = -\frac{1}{4} |p_1|^2 \nabla \kappa_0 - \frac{1}{4} |v_1|^2 \nabla \rho_0. \quad (2.20)$$

This force is discussed in detail in Chap. 4.

## Chapter 3

# Numerical simulations with COMSOL Multiphysics

Many governing equations of continuum physics exhibit a common structure, which can be described by the following general form:

$$\nabla \cdot \mathbf{J} [u(\mathbf{r}, t)] - F [u(\mathbf{r}, t)] = 0 \quad \text{for } \mathbf{r} \in \Omega, \quad (3.1)$$

in which a net outflow rate  $\nabla \cdot \mathbf{J}$  of some generalized flux  $\mathbf{J}$  is equated to a generalized source or forcing term  $F$ . This equation, together with boundary conditions for specifying its solutions on the boundary  $\partial\Omega$  of the continuous domain  $\Omega$ , represents the strong formulation of a boundary-value problem.

The so-called strong solution  $u$  satisfies Eq. (3.1) over all of domain  $\Omega$ , including the specified conditions on boundary  $\partial\Omega$ . Obtaining these solutions, however, is seldom feasible and typically limited to cases involving remarkably simple geometries and symmetries. Consequently, we turn to numerical simulations on our powerful modern computers to find approximate solutions instead. The purpose of this chapter is to introduce the reader to the numerical simulation package COMSOL Multiphysics 6.1, which employs the finite element method for obtaining these approximate solutions. The chapter covers topics such as the weak formulation of a partial differential equation (PDE), boundary conditions, symmetries, and mesh quality studies, all of which are familiar to anyone engaged with finite-element modeling. The chapter is mostly based on Refs. [16, 21].

### 3.1 Finite element method

Due to the constraints of computer memory and the infinite number of degrees of freedom involved, the problems needs to be discretized into a finite number of degrees of freedom. COMSOL achieves this using the finite element method, in which the continuous domain  $\Omega$  is discretized by a mesh, and the physical fields and PDEs are represented using interpolating polynomial functions, which act as probes on the

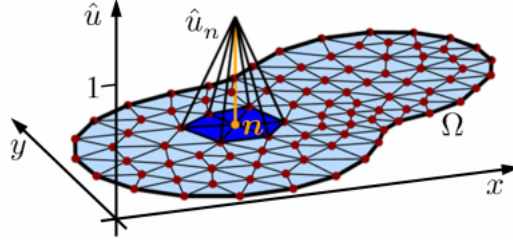


Figure 3.1: The 2D domain  $\Omega$  is discretized by a triangular mesh. The mesh is composed of vertices (red points) and mesh elements (light blue domains). The  $n$ th mesh cell (dark blue) with its center point (yellow point) in  $\mathbf{r}_n$  and test function  $\hat{u}_n$ , is shown. Adapted from Ref. [21].

discretized domain. This representation is known as the weak formulation.

### 3.1.1 Discretization

The mesh is generated from a finite number  $N$  of points  $\mathbf{r}_n \in \Omega$ ,  $n = 1, 2, \dots, N$ . The points serve as the vertices for the elements of the mesh. The collection of elements with  $\mathbf{r}_n$  as a vertex constitute the  $n$ th mesh cell, which is associated with the test function  $\hat{g}_n$  representing the probe on the cell.

The test functions are piecewise polynomial functions with compact support on their respective cells. The functions constitute a finite basis, by which the physical fields can be approximated as

$$u(\mathbf{r}) \approx \sum_{n=1}^N c_n \hat{u}_n(\mathbf{r}). \quad (3.2)$$

Here,  $c_n$  are unknown coefficients to be computed numerically. The degrees of freedom have thus reduced to these coefficients. For increasing orders of the polynomials, the number of degrees of freedom increases, but so does the accuracy of this representation.

### 3.1.2 The weak formulation of a PDE

Substituting for  $u$  in Eq. (3.1) from Eq. (3.2) yields a non-zero residual,

$$d(\mathbf{r}) = \nabla \cdot \mathbf{J}[u(\mathbf{r})] - F[\mathbf{r}, u(\mathbf{r})]. \quad (3.3)$$

In order that Eq. (3.1) is approximately satisfied, the coefficients  $c_n$  are chosen such that the mean of this residual over each mesh cell vanishes,

$$\int_{\Omega} \hat{u}_m (\nabla \cdot \mathbf{J} - F) dV = 0 \quad \text{for all } m. \quad (3.4)$$

This equation is known as the weak formulation of Eq. (3.1).

For linear flux and force operators, the foregoing equation leads to a system of algebraic equations that can be solved for the coefficients  $c_n$ . By defining the matrix elements

$$K_{mn} = \int_{\Omega} \hat{u}_m \left\{ \nabla \cdot \mathbf{J}[\hat{u}_n] - F[\hat{u}_n] \right\} dV, \quad (3.5)$$

Eq. (3.4) simplifies to

$$\sum_n K_{mn} c_n = 0. \quad (3.6)$$

### 3.1.3 Boundary conditions on weak form

The predominant types of boundary conditions are the Dirichlet condition and the Neumann condition. These conditions specify the values that the solution  $u$  and the normal flux  $(\hat{\mathbf{n}} \cdot \nabla)u$  must take on the domain boundary  $\partial\Omega$ , respectively:

$$u(\mathbf{r}) = D(\mathbf{r}) \quad \text{for } \mathbf{r} \in \partial\Omega \quad (\text{Dirichlet boundary condition}), \quad (3.7a)$$

$$(\hat{\mathbf{n}} \cdot \nabla)u(\mathbf{r}) = N(\mathbf{r}) \quad \text{for } \mathbf{r} \in \partial\Omega \quad (\text{Neumann boundary condition}), \quad (3.7b)$$

with  $\hat{\mathbf{n}}$  being the outwards pointing unit normal on  $\partial\Omega$ .

To see how we implement these conditions in the weak form, we transform Eq. (3.4) by application of the product rule of differentiation,  $\hat{u}_m \nabla \cdot \mathbf{J} = (\nabla \hat{u}_m) \cdot \mathbf{J} - \nabla \cdot (\hat{u}_m \mathbf{J})$ , and Gauss's theorem,  $\int_{\Omega} \nabla \cdot (\hat{u}_m \mathbf{J}) dV = \oint_{\partial\Omega} \hat{u}_m (\hat{\mathbf{n}} \cdot \mathbf{J}) dA$ , to reveal the flux crossing the domain boundary,

$$\int_{\partial\Omega} \hat{u}_m \hat{\mathbf{n}} \cdot \mathbf{J} dA + \int_{\Omega} [(-\nabla \hat{u}_m) \cdot \mathbf{J} - \hat{u}_m F] dV = 0. \quad (3.8)$$

In this equation, the current that passes through the boundary due to a normal flux  $\hat{\mathbf{n}} \cdot \mathbf{J}$  is identified by the surface integral. A Neumann condition is thus imposed by specifying the integrand of this integral:  $\hat{\mathbf{n}} \cdot \mathbf{J} = N$ .

Other types of boundary conditions, generally written as  $R[u(\mathbf{r}), \mathbf{J}(\mathbf{r})] = 0$ , is implemented by introducing to the boundary an auxiliary field  $\lambda$  and its corresponding set of test functions  $\hat{\lambda}_m$ . This turns the foregoing equation into

$$\int_{\partial\Omega} \left\{ \hat{u}_m \lambda + \hat{\lambda}_m R[u, \mathbf{J}] \right\} dA + \int_{\Omega} [(-\nabla \hat{u}_m) \cdot \mathbf{J} - \hat{u}_m F] dV = 0. \quad (3.9)$$

A Dirichlet condition is imposed by choosing  $R[u, \mathbf{J}] = D - u$  and specifying  $D$ . The Lagrange multiplier  $\lambda$  can be identified as the flux that maintains this value of  $u$  on the boundary.

### 3.1.4 Symmetry conditions

Systems may exhibit symmetries such as mirror plane symmetry and mirror plane anti-symmetry. Symmetries imply that certain conditions are satisfied within the plane of symmetry. Enforcing these conditions as boundary conditions on the symmetry planes allows us to reduce the size of the model, saving both computational time and memory.

Mirror plane symmetry refers to the property of a field being symmetric under a reflection through a plane—the symmetry plane. The symmetry corresponds to the normal derivative of the field vanishing in the plane. Thus, to implement this symmetry, we impose a no-flux condition [Neumann condition (3.7b) with  $N = 0$ ] on the symmetry plane:

$$(\hat{\mathbf{n}} \cdot \nabla)u = 0 \quad (\text{mirror plane symmetry}). \quad (3.10)$$

Conversely, a mirror plane anti-symmetry indicates that a field is anti-symmetric under a reflection through the symmetry plane. In the case of this symmetry, the field value need to vanish on the symmetry plane [Dirichlet condition (3.7a) with  $D = 0$ ]:

$$u = 0 \quad (\text{mirror plane anti-symmetry}). \quad (3.11)$$

## 3.2 Numerical stability and mesh refinement study

### 3.2.1 Stability criteria

When constructing a mesh for a problem involving advection, it is important to consider the cell Péclet number  $Pe_{\text{cell}}$ . This Péclet number, defined by

$$Pe_{\text{cell}} = \frac{U h_{\text{mesh}}}{D}, \quad (3.12)$$

with  $U$  being the advective velocity,  $h_{\text{mesh}}$  the size of mesh elements, and  $D$  the diffusivity, should not exceed a value of 2 to ensure numerical stability. [22]

Another important dimensionless quantity is the Courant number  $Co$ , which relates the temporal resolution represented by the time step size  $\Delta t$  of the solver and the spatial resolution represented by  $h_{\text{mesh}}$ . The Courant number is defined as

$$Co = \frac{U \Delta t}{h_{\text{mesh}}}. \quad (3.13)$$

To ensure stability,  $Co$  should not exceed 1, but it is advisable that it should be much smaller. We generally aim for one that is 0.1 at most.

Using these criteria, appropriate values for the mesh element size  $h_{\text{mesh}}$  and the time step size  $\Delta t$  for ensuring numerical stability and accuracy can be estimated. For highly advective problems, it can be advantageous to increase the order of the interpolating polynomials instead of making the mesh finer in

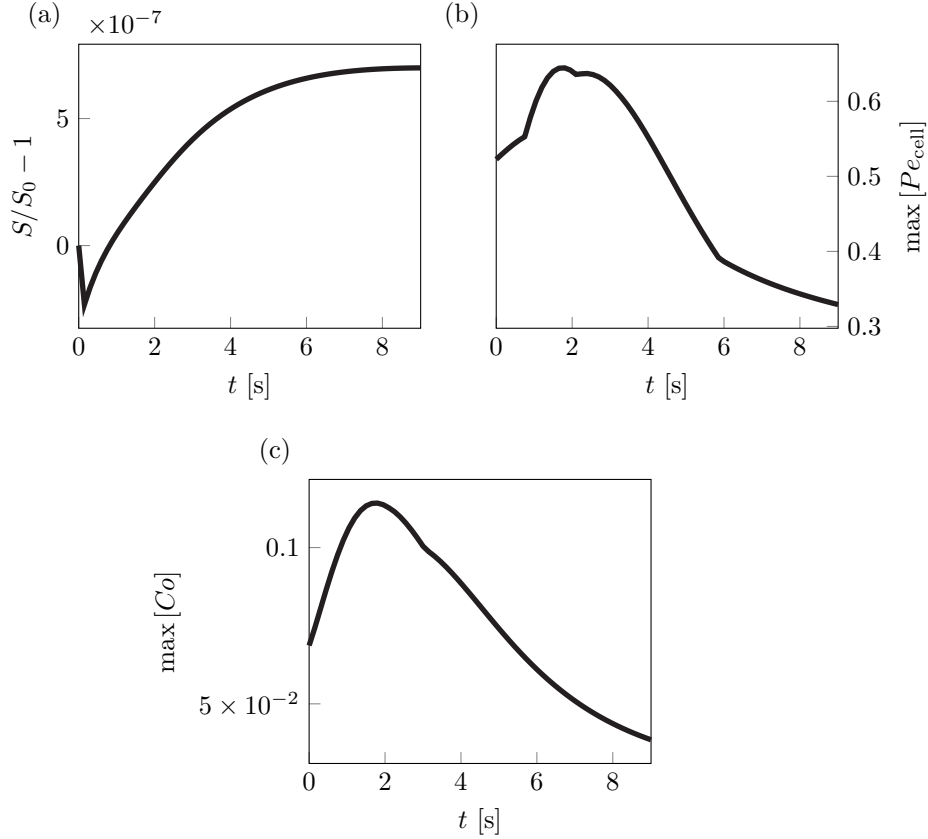


Figure 3.2: Results of probes for a 2D simulation with the parameters values given in Tab. 4.1. (a) The relative difference of the amount of solute  $S$  from the initial amount  $S_0$  vs. time. (b)–(c) The maximum cell Péclet number and the maximum Courant number vs. time.

order to avoid absurdly small  $h_{\text{mesh}}$  and hence  $\Delta t$ . This is possible because raising the polynomial order effectively introduces additional (invisible) nodes that reduces  $Pe_{\text{cell}}$  without making the mesh elements smaller.

### 3.2.2 Probes

A number of probes are implemented to keep track of parameters that indicate mesh quality. The first probe integrates  $s$  over the entire domain,

$$S = \int_{\Omega} s dV, \quad (3.14)$$

to ensure that mass is conserved. Figure 3.2(a) shows the relative mass-fluctuation  $S/S_0 - 1$ , with  $S_0 = S(t=0)$ , vs. time for a 2D simulation. The mass is conserved within margins of 0.0001%.

Two other probes calculated the maximum cell Péclet number,  $\max[Pe_{\text{cell}}]$ , and the maximum

Courant number,  $\max[Co]$ , ensuring that the spatiotemporal resolution is sufficient. The numbers were evaluated as

$$Pe_{\text{cell}} = \frac{|\mathbf{v}|h_{\text{mesh}}}{p_s D}, \quad Co = \frac{|\mathbf{v}|\Delta t}{h_{\text{mesh}}}, \quad (3.15)$$

with  $|\mathbf{v}|$  being the local velocity magnitude at a given time,  $h_{\text{mesh}}$  the local mesh element size, and  $p_s = 3$  the polynomial order of  $s$ . Figure 3.2(b)–(c) show the maximum of these quantities for the same 2D simulation. Both numbers were well below their critical values of 2 and 1, respectively.

### 3.2.3 Mesh refinement study

A mesh refinement study is conducted to ensure that simulation results are reliable and independent of the mesh used. The study involves computing the solution on progressively finer meshes. As the mesh is refined, the solution improves and approaches the true solution of the problem. Using the solution on the finest mesh as a reference, the convergence of the mesh is quantified by the discrepancy  $\mathcal{D}$  of the solution on some given mesh, measured by the normalized  $L^2$ -norm:

$$\mathcal{D} = \sqrt{\frac{\int_{\Omega} |u - u_{\text{ref}}|^2 dV}{\int_{\Omega} |u_{\text{ref}}|^2 dV}}. \quad (3.16)$$

To refine the mesh, a mesh refinement factor  $CONV$  was introduced. This parameter enters as a factor on the mesh element size  $h_{\text{mesh}}$  and is increased to refine the mesh.

The results of conducting a mesh refinement study is shown in Fig. 3.3. For most applications of numerical models, a margin of error  $< 1\%$  is sufficient. We find that all errors are well below this threshold. Linear regions indicate exponential convergence. The computation times ranged between 2 minutes on the coarsest of meshes (DOF 16,218) and 4 hours on the finest of meshes (DOF 478,077).

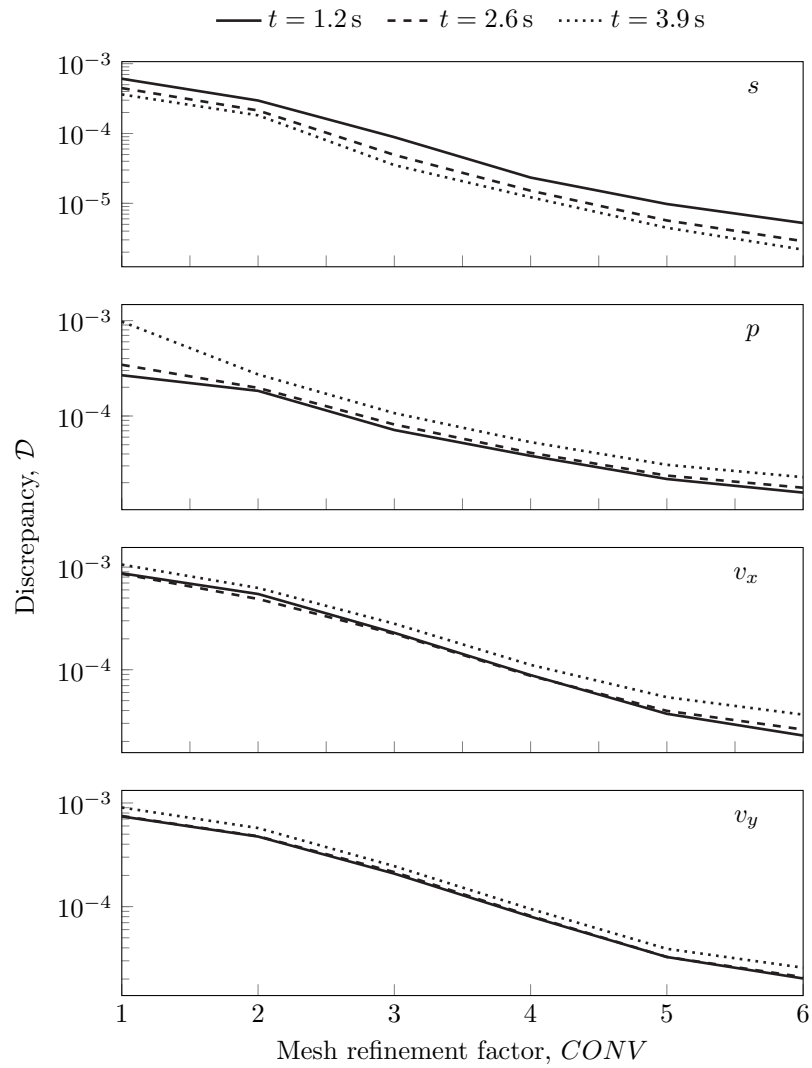


Figure 3.3: Plot of the discrepancy,  $\mathcal{D}$ , vs. mesh refinement factor,  $CONV$ , for a 2D simulation with parameter values given in Tab. 4.1. Line types (solid, dashed, dotted) represent times  $t = 1.2, 2.6, 3.9$  s. Running times range between minutes for the coarsest of meshes and hours for the finest.



# Chapter 4

## The 3D model

In this chapter, we lay the groundwork for the numerical model that serve as the foundation for subsequent chapters. We begin by making general observations regarding the patterning process and, based on preliminary simulations and order-of-magnitude calculations, derive a simplified set of equations describing this process for simulating it in 3D. To facilitate the 3D simulation, we exploit every symmetry inherent in the problem and confine the computational domain to one that is much smaller than the microfluidic chamber. The details of this implementation is the subject of Sec. 2. Finally, we present and discuss the results obtained from the simulation in Sec. 3.

Moreover, to maintain clarity and avoid notational clutter or conflicts, we abandon the numeral subscripts to denote acoustics fields and adopt a subscript ‘ac’ instead.

### 4.1 Formulation of 3D model

We consider a shallow microfluidic chamber of length  $L = 8000\ \mu\text{m}$ , width  $W = 1500\ \mu\text{m}$ , and height  $2h = 40\ \mu\text{m}$ , as sketched in Fig. 4.1. Within this chamber, there is an inhomogeneous solution of Ficoll PM400 in water, characterized by the concentration-dependencies of its density  $\rho$ , viscosity  $\eta$ , sound

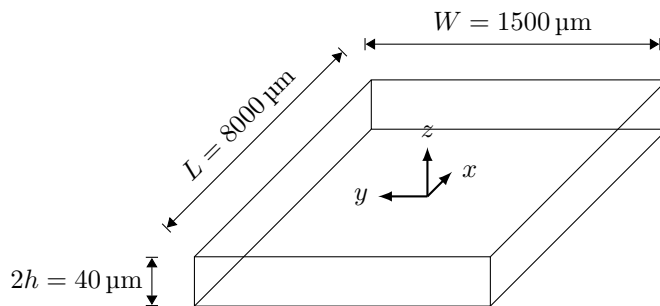


Figure 4.1: Sketch of microfluidic chamber of length  $L$ , width  $W$ , and height  $2h$ .

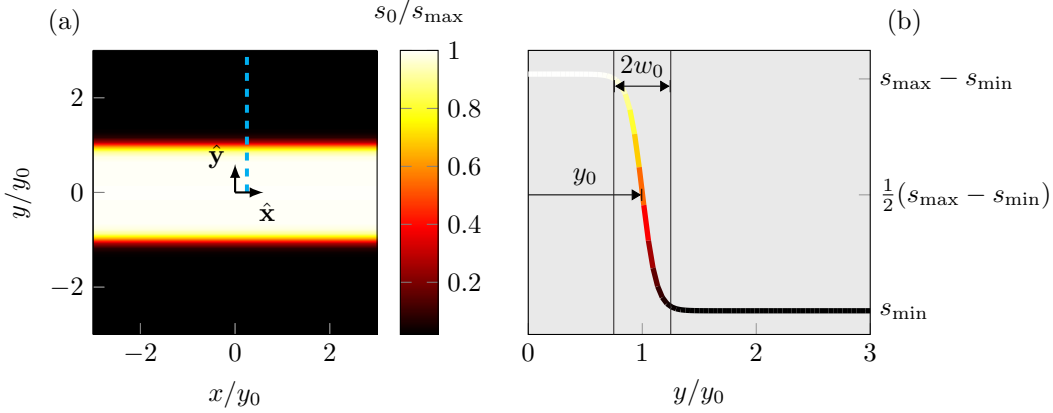


Figure 4.2: Initial solute concentration field  $s_0$  given by Eq. (4.1). (a) Surface plot of  $s_0$ . The solute band extends infinitely along the  $x$ -axis. (b) Concentration profile evaluated along the dashed line in panel (a). The parameter  $y_0$  represents the half-width of the profile, measuring the width between the longitudinal axis at the maximum value and the point at half maximum. The parameter  $w_0$  represents the interfacial slope between solute and solvent.

speed  $c$ , and diffusivity  $D$  given in Eq. 2.9.

The initial configuration of the solution is described by the following concentration profile  $s_0$ , resembling an infinitely long band positioned along the longitudinal axis (the  $x$ -axis) of the chamber:

$$s_0 \equiv s(x, y, z, t = 0) = s_{\min} + \frac{1}{4}(s_{\max} - s_{\min}) \left[ 1 + \tanh\left(\frac{y + y_0}{w_0/2}\right) \right] \left[ 1 + \tanh\left(\frac{y_0 - y}{w_0/2}\right) \right]. \quad (4.1)$$

with  $s_{\max}$  being the maximum concentration,  $s_{\min}$  the minimum concentration,  $y_0$  the width, and  $w_0$  the initial gradient width representing the initial concentration gradient scale,  $|\nabla s_0| \sim s_{\max}/w_0$ . If  $y_0 \gg w_0$ ,  $y_0$  is identical to the half width at half maximum. The concentration profile is shown in Fig. 4.2.

A propagating acoustic vortex impinges on the chamber containing the solution from below. Based on experimental observations and simulations of the acoustic pressure field inside the chamber, the field is approximated by a spherical Bessel function of topological charge  $\ell = 1$ ,

$$p_{\text{ac}} = \frac{p_{\text{ac}}^{\max}}{j_1^{\max}} j_1(kr) e^{i(\theta - \omega t)}, \quad (4.2)$$

with  $(r, \theta)$  being cylindrical polar coordinates<sup>1</sup>,  $p_{\text{ac}}^{\max}$  the maximum acoustic pressure,  $j_\ell$  the spherical Bessel function of order  $\ell$  and  $j_\ell^{\max}$  its maximum,  $\omega$  being the angular frequency and  $k$  the lateral wave number [7]. Notably, this pressure field is uniform in the height of the chamber. The maximum acoustic pressure can be estimated using the traveling wave formula,  $p_{\text{ac}}^{\max} \sim \rho_w c_g v_n^{\max} = \rho_w c_g \omega d_n^{\max}$ , with  $c_g = 3500 \text{ m s}^{-1}$  being the transverse speed of sound in the glass slide on the bottom of the chamber,  $v_n^{\max} = \omega d_n^{\max}$  the maximum normal velocity at the boundary between the glass slide and the chamber,

<sup>1</sup> $\theta$  is equivalent to the azimuthal angle  $\varphi$  in spherical coordinates.

$d_n^{\max}$  the maximum normal displacement of this boundary, and  $f = \omega/2\pi = 17.3$  MHz the driving frequency. In experiments,  $d_n^{\max}$  typically vary between 0.1 and 1 nm; for the intermediate value of 0.5 nm, the maximum acoustic pressure measures 0.19 MPa. The wave number is estimated by  $k = \omega/c_g$ , corresponding to the wavelength  $\lambda = c_g/f \approx 202 \mu\text{m}$  [7]. The pressure field has been shown in Fig 4.3(a)–(b). It resembles a rotating acoustic dipole with angular frequency  $\omega$ . The topological charge indicates the number of nodal lines in the field. For  $\ell = 1$ , a single nodal line passes through the center directly between the two poles.

The corresponding acoustic velocity is obtained by the linearized Navier–Stokes equations (2.16b), the result being

$$\mathbf{v}_{\text{ac}} = -\frac{\text{i}}{kc_w\rho_w} \frac{p_{\text{ac}}^{\max}}{j_1^{\max}} \left[ \left( j_0(kr) - \frac{2}{kr} j_1(kr) \right) \hat{\mathbf{r}} + \frac{\text{i}}{kr} j_1(kr) \hat{\boldsymbol{\theta}} \right] e^{\text{i}(\theta - \omega t)}, \quad (4.3)$$

in which  $\hat{\mathbf{r}}$  and  $\hat{\boldsymbol{\theta}}$  are the unit vectors for cylindrical polar coordinates.

In presence of the acoustic field, the acoustic body force  $\mathbf{f}_{\text{ac}}$  arises on the inhomogeneous solution due to the gradients in its density and compressibility, as given by Eq. (2.20). In terms of  $s$ , this force may be written as

$$\mathbf{f}_{\text{ac}} = -\frac{1}{4} \left[ \left( \frac{\partial \kappa}{\partial s} \right)_T |p_{\text{ac}}|^2 + \left( \frac{\partial \rho}{\partial s} \right)_T |\mathbf{v}_{\text{ac}}|^2 \right] \nabla s, \quad (4.4)$$

with the subscript  $T$  in  $(\partial \kappa / \partial s)_T$  and  $(\partial \rho / \partial s)_T$  denoting that temperature is held constant. From the expressions in Eq. (2.9), the derivatives can be evaluated to be

$$\frac{1}{\kappa_w} \left( \frac{\partial \kappa}{\partial s} \right)_T = -a_1 - 2c_1 \quad \text{and} \quad \frac{1}{\rho_w} \left( \frac{\partial \rho}{\partial s} \right)_T = a_1, \quad (4.5)$$

to lowest order in  $s$ . (If  $s_{\max} \sim 0.1$ , the magnitude of errors associated in making this approximation is on the order of  $a_1^2 s_{\max} \sim 0.01$ .<sup>2</sup>) The solute-induced acoustic body force (4.4) thus becomes

$$\mathbf{f}_{\text{ac}} = F_{\text{ac}} \nabla s, \quad F_{\text{ac}} \equiv \frac{1}{4} [\kappa_w (a_1 + 2c_1) |p_{\text{ac}}|^2 - \rho_w a_1 |\mathbf{v}_{\text{ac}}|^2], \quad (4.6)$$

in which  $F_{\text{ac}}$  is referred to as the force-shape function, representing the shape of the force independent of concentration gradients.

The force-shape function  $F_{\text{ac}}$  has been shown in Fig. 4.3(c)–(d). In Fig. 4.3(c), it is shown in the  $xy$ -plane, centered at the center of the acoustic vortex. Being independent of the angle  $\theta$ ,  $F_{\text{ac}}$  is circular symmetric in contrast to the vortex. In Fig. 4.3(d),  $F_{\text{ac}}$  is shown vs. the normalized radial distance  $kr$ . The gray lines represent the individual terms of the function, including the acoustic pressure (solid) and the acoustic velocity (dashed). For  $a_1$  and  $c_1$  given in Tab. 2.1, the pressure term is responsible for the force pointing in the direction of increasing solute concentration near acoustic pressure maxima, whereas the velocity term is responsible for the force pointing in the direction of decreasing concentration near acoustic pressure nodes. Asymptotically,  $F_{\text{ac}}$  decays like  $(kr)^{-2}$ , leading to  $\mathbf{f}_{\text{ac}}$  being highly localized at

<sup>2</sup>For example,  $(1/\rho)(\partial \rho / \partial s)_T = a_1 / (1 + a_1 s) \simeq a_1 - a_1^2 s + O(s^2)$ , leading to this error estimate.

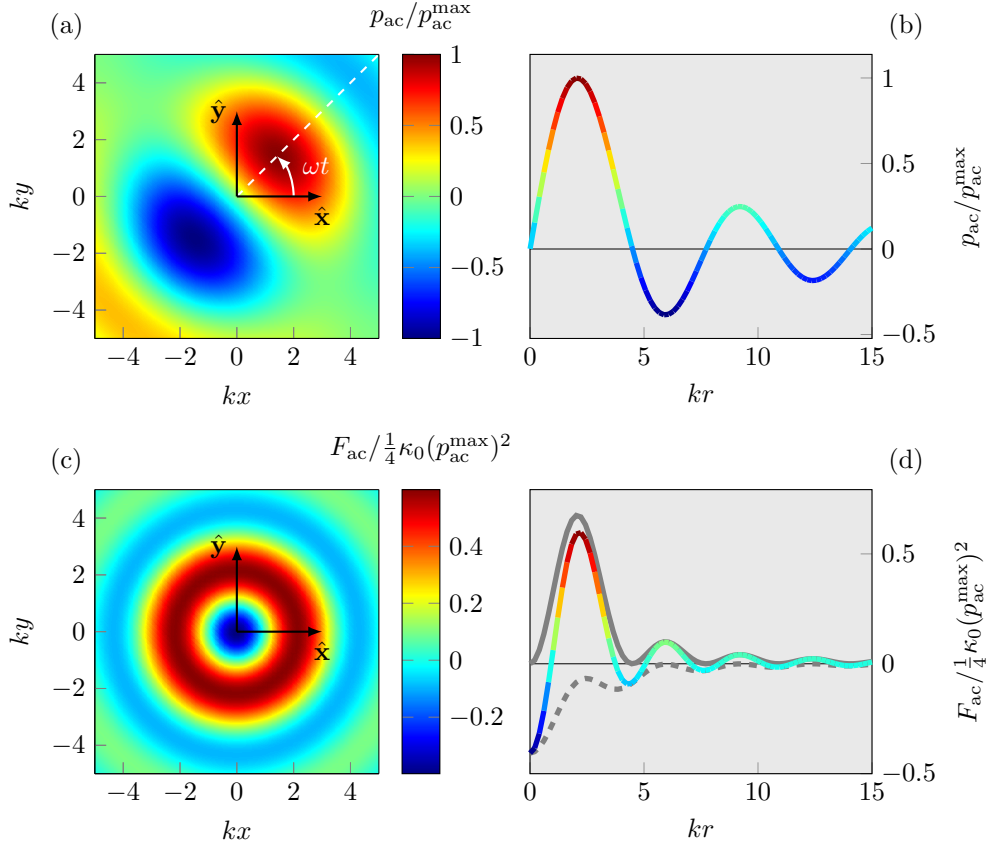


Figure 4.3: Acoustic pressure (4.2) and acoustic shape-function (4.6). (a) The acoustic pressure in the  $xy$ -plane, rotated around the out-of-plane  $z$ -axis after a time  $t$ . (b) The acoustic pressure evaluated along white dashed line in panel (a). (c) The acoustic shape-function in the  $xy$ -plane. (d) Acoustic shape-function (black) evaluated along any arbitrary radial direction. The solid gray line represents the term due to acoustic pressure; the dashed gray line represents the term due to acoustic velocity.

the acoustic center.

We now develop the governing equations describing the patterning of the Ficoll solution. Our starting point is the equation of incompressibility, the Navier–Stokes equations, and the convection-diffusion equation:

$$0 = \nabla \cdot \mathbf{v}, \quad (4.7a)$$

$$\rho \partial_t \mathbf{v} + \rho (\mathbf{v} \cdot \nabla) \mathbf{v} = -\nabla p + \nabla \cdot \boldsymbol{\tau} + \rho \mathbf{g} + \mathbf{f}_{ac}, \quad (4.7b)$$

$$\partial_t s + (\mathbf{v} \cdot \nabla) s = \nabla \cdot (D \nabla s), \quad (4.7c)$$

in which  $\mathbf{g} = -g\hat{\mathbf{z}}$  is the acceleration due to gravity, and the viscous stress tensor  $\boldsymbol{\tau}$  is given by

$$\boldsymbol{\tau} = \eta [\nabla \mathbf{v} + (\nabla \mathbf{v})^T], \quad (4.8)$$

valid for incompressible flows of Newtonian fluids.

We consider the importance of the individual terms in the Navier–Stokes equations (4.7b). We start with the gravitational term  $\rho\mathbf{g}$  and put  $\mathbf{f}_{\text{ac}} = \mathbf{0}$ . Using the expression for the density  $\rho$  given in Eq. (2.9) and absorbing the constant part of gravitational terms in the pressure gradient, the resulting Navier–Stokes equations are

$$\rho\partial_t\mathbf{v} + \rho(\mathbf{v} \cdot \nabla)\mathbf{v} = -\nabla p + \nabla \cdot \boldsymbol{\tau} + \rho_w a_1 s \mathbf{g}. \quad (4.9)$$

The initial configuration (4.1) of the fluids does not describe a state of hydrostatic equilibrium in which the density gradient must be parallel to the axis of gravity. The gravitational term  $\rho_w a_1 s \mathbf{g}$  in the foregoing equation therefore leads to convection, resulting in the Ficoll solution settling at the bottom of the chamber. However, preliminary simulations show that this convective rearrangement is negligible with variations only amounting to 3%, measured by the normalized  $L^2$ -norm relative to the height-averaged concentration value. This variation subsequently decayed over time due to diffusion.

A major contributing factor to convection being negligible is the chamber’s shallowness. The convective speed is limited by the rate, at which solute and solvent can replace one another in the height. The volumetric flow rates of the two need be balanced due to volume conservation of incompressible flows. This requirement leads to the following relationship between the vertical velocity,  $v_z$ , at which solute settles at the bottom, and the horizontal velocity,  $v_y$ , at which the solvent is pushed out:  $v_z = (h/y_0)v_y$ , implying that wide solute bands experience less convection. This relationship was confirmed in the simulations. Thus, the influence of gravity is neglected, and Eq. (4.7c) is referred to as the advection-diffusion equation.

Next we consider the inertial terms  $\rho\partial_t\mathbf{v}$  and  $\rho(\mathbf{v} \cdot \nabla)\mathbf{v}$  on the left-hand sides of the Navier–Stokes equations. With the acoustic patterning of the solution occurring on the time scale of 1 s, as observed in the experiments carried out by Almohamad et al. [14], the effective Reynolds number<sup>3</sup> is  $\sim 0.001 \ll 1$ , with  $h \sim 10 \mu\text{m}$ ,  $\eta \sim 1 \text{ mPa}\cdot\text{s}$ , and  $\rho \sim 1000 \text{ kg m}^{-3}$ . Consequently, both inertial terms are negligible, and the acoustic-induced flow is governed by a set of quasi-static Stokes equations with the acoustic force density (4.6) serving as driving force. Although this acoustic force density exhibits time-dependency through the gradient of the concentration  $\nabla s$ , the explicit time-dependency of  $\mathbf{v}$  can be disregarded, because  $\mathbf{v}$  responds to any change in  $\mathbf{f}_{\text{ac}}$  so rapidly that, on the time scale of observation, that response can be considered instantaneous.

Thus, the set of equations that governs the acoustic patterning of Ficoll PM400 consists of the in-

---

<sup>3</sup>Effective in the sense that we actually are calculating  $(h/L)Re$ , with  $h$  and  $L$  being the characteristic lengths of the vertical and lateral dimensions and  $Re$  the actual Reynolds number calculated with  $h$ .

compressibility equation, the quasi-static Stokes equations, and the advection-diffusion equation:

$$\nabla \cdot \mathbf{v} = 0, \quad (4.10a)$$

$$0 = -\nabla p + \nabla \cdot \boldsymbol{\tau} + F_{\text{ac}} \nabla s, \quad (4.10b)$$

$$\partial_t s + (\mathbf{v} \cdot \nabla) s = \nabla \cdot (D \nabla s), \quad (4.10c)$$

in which we have substituted for  $\mathbf{f}_{\text{ac}}$  from Eq. (4.6). These equations are to be solved with the no-slip condition for the velocity and the no-flux condition for the solute on the chamber walls:

$$\mathbf{v} = \mathbf{0}, \quad (4.11)$$

$$(\hat{\mathbf{n}} \cdot \nabla) s = 0. \quad (4.12)$$

Furthermore, it is useful to define the following quantities. There is the advective time scale of mass transport,

$$\tau_{\text{adv}} = \frac{1}{U_0 k} \approx t^*, \quad (4.13)$$

expressing the time of mass transport by advection on the length scale of the acoustics. We approximate this quantity by the patterning time  $t^*$  for performing fast calculations.

Then, there is the ‘long’ diffusive time scale calculated using  $1/k$  as characteristic length scale,

$$\tau_{\text{diff}}^{\parallel} = \frac{1}{D_w k^2} \approx 9 \text{ s}. \quad (4.14)$$

This time scale approximates the diffusive decay time of the pattern and thus its life-time. This time scale is relevant when examining the concentration contrast,  $C$ .

Conversely, the ‘short’ diffusive time scale using  $h$  as characteristic length is

$$\tau_{\text{diff}} = \frac{h^2}{D_w} \approx 3.5 \text{ s}. \quad (4.15)$$

The ratio of  $\tau_{\text{diff}}$  and  $\tau_{\text{adv}}$  is the effective Péclet number,

$$Pe_{\text{eff}} = \frac{\tau_{\text{diff}}}{\tau_{\text{adv}}} \approx \frac{\tau_{\text{diff}}}{t^*}, \quad (4.16)$$

whence we can calculate the Péclet number as

$$Pe = (kh)^{-1} Pe_{\text{eff}}. \quad (4.17)$$

Here, the dimensionless quantity formed by  $kh$  expresses the disparity between the characteristic lengths  $h$  and  $1/k$ , leading us to define the acoustic aspect ratio  $\epsilon$ :

$$\epsilon \equiv kh = 0.62. \quad (4.18)$$

Table 4.1: Default parameter values of the acoustics, the Ficol solution, and the geometry.

<i>Acoustic parameters</i>			<i>Solute parameters</i>			<i>Geometry</i>		
Symbol	Value	Units	Symbol	Value	Units	Symbol	Value	Units
$f$	17.3	MHz	$s_{\max}$	0.05	1	$h$	20	$\mu\text{m}$
$c_g$	3500	$\text{m s}^{-1}$	$s_{\min}$	0.001	1	$R$	370	$\mu\text{m}$
$d_n^{\max}$	0.5	nm	$y_0$	90	$\mu\text{m}$	$R_1$	163	$\mu\text{m}$
$p_{\text{ac}}^{\max}$	0.19	MPa	$w_0$	36	$\mu\text{m}$	$R_2$	268	$\mu\text{m}$
$\lambda$	202	$\mu\text{m}$						

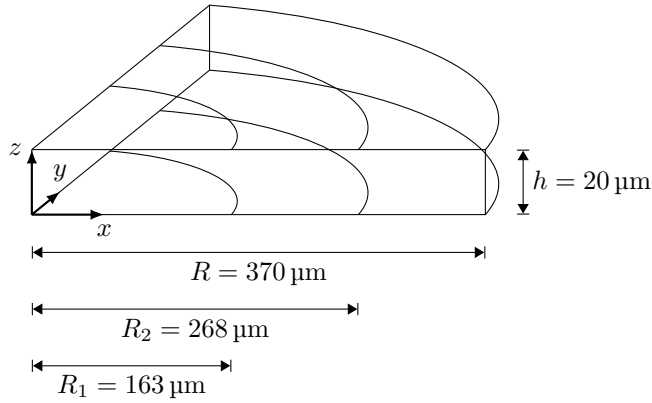


Figure 4.4: Sketch of geometry. By exploiting symmetries of the system and the radial decay of the acoustic force density, the computational domain have been reduced from the microfluidic chamber to the quarter of cylinder. This domain is partitioned into 3 segments by the radii  $R_1$  and  $R_2$ , used for meshing.

Finally, we define the height-average operation:

$$\langle f \rangle(x, y, t) = \frac{1}{2h} \int_{-h}^h f(x, y, z, t) dz. \quad (4.19)$$

This operation projects the fields onto the 2D  $xy$ -plane. In experimental setups, like the one depicted in Fig. 1.1, the  $z$ -dimension is not resolved, and the measured quantities correspond to their height-averaged values.

## 4.2 Model implementation

We now implement the model formulated in the previous section using COMSOL's Weak Form PDE interface. For the governing equations (4.10), we write down the generalized forces and fluxes, the result

being

$$F = \nabla \cdot \mathbf{v}, \quad \mathbf{J} = \mathbf{0}; \quad (4.20a)$$

$$\mathbf{F} = -F_{\text{ac}} \nabla s, \quad \mathbf{J} = -p\mathbf{I} + \eta [\nabla \mathbf{v} + (\nabla \mathbf{v})^T]; \quad (4.20b)$$

$$F = -\partial_t s - (\mathbf{v} \cdot \nabla) s, \quad \mathbf{J} = -D \nabla s, \quad (4.20c)$$

in which the parameters  $\rho$ ,  $\eta$ ,  $c$ ,  $D$  are given in Eq. (2.9). The acoustic fields enters through the acoustic force-shape function,  $F_{\text{ac}}$ , which is implemented analytically. Furthermore, to improve numerical stability, the solute concentration field  $s$  is represented by its logarithm  $\ln(s)$ . Whereas  $s$  always is positive,  $\ln(s)$  can take negative values, circumventing the problem of concentration values becoming negative due to numerical imprecision, which would be fatal to the simulations.

The microfluidic chamber is too large to simulate in its entirety, because it requires millions of mesh elements to meet the condition of the cell Péclet number,  $Pe_{\text{cell}} = |\mathbf{v}|h_{\text{mesh}}/D < 2$ . Considering  $D \sim 1 \times 10^{-10} \text{ m}^2 \text{ s}^{-1}$  and  $|\mathbf{v}| \sim \lambda/1 \text{ s} \sim 200 \mu\text{m s}^{-1}$ , with 1 s being the patterning time, the mesh element size is  $h_{\text{mesh}} \sim 1 \mu\text{m}$ . As a result, the number of mesh elements exceeds 400,000,000, and the number of degrees of freedom is even greater. Therefore, instead of modeling the entire chamber, we limit the computational domain to a small cylindrical region of radius  $R$  centered at the acoustic center. Within this region, the acoustic force density is greatest, and the cylindrical shape respects the circular symmetry of the force-shape function. However, introducing artificial outer boundaries in this manner is going to produce errors. To minimize these errors, the radius  $R$ , at which the boundary is positioned, is chosen such that  $R$  is sufficiently large for the force-shape function  $F_{\text{ac}}$  to have decayed by a factor of 100, i.e.,  $(kR)^{-2} < 0.01$ , and corresponds to a node of the force-shape function,  $F_{\text{ac}}(kR) = 0$ . Based on these criteria,  $R$  is determined to be  $11.5k^{-1}$ . By reducing the domain to this cylinder, we achieve a relative volume-reduction of  $\pi R^2/WL - 1 > 0.8$ , with  $L > W$ . Furthermore, employing the invariance of the Ficoll band (4.1) to translations along the  $x$ -axis (and circular symmetry of  $F_{\text{ac}}$ ) and the symmetry of the problem along the  $z$ -axis, this volume is reduced by a factor 1/4. Moreover, if we position the acoustic center along the longitudinal axis of the solute band, this volume can be halved due to the symmetry across the longitudinal axis. The final geometry is shown in Fig. 4.4.

Regarding mesh, we take advantage of the radial decay of the acoustic force density and increase the mesh element size radially. To achieve this, the cylindrical domain is partitioned into three layers by the internal radii  $R_1$  and  $R_2$ , coinciding with nodes of the force-shape function. The mesh element size  $h_{\text{mesh},1}$  within the first layer of radius  $R_1$  is set to scale with a characteristic speed  $U_0$  obtained by balancing magnitude of the acoustic force density with that of viscosity:  $U_0 = (K/4)\kappa_w(j_1^{\text{max}}p_{\text{ac}}^{\text{max}})^2 s_{\text{max}} h/\eta_0$ , where  $K$  is a dimensionless constant determined by a mesh refinement study.<sup>4</sup> The mesh element sizes within the subsequent layers are set to  $(kR_1)h_{\text{mesh},1}$  and  $(kR_2)h_{\text{mesh},1}$ , respectively, with maximum element growth rates of 1.2 and curvatures of 0.3. This mesh is then extruded throughout the domain with 3 layers in the height. The initial time step is set to  $1 \times 10^{-6} \text{ s}$ , and the maximum time step  $\Delta t$  is  $0.05h_{\text{mesh},1}/U_0 \sim 0.01 \text{ s}$ . For the parameter values given in Tab. 4.1, the number of degrees of freedom

<sup>4</sup>Namely,  $K = \text{CONV}/40$ , where 40 was chosen to scale  $U_0$  down to the observed speeds.

become 603,350, and the solution time is 3 hours.

### 4.3 Results and discussion

Figure 4.5 shows the simulated patterning of Ficoll PM400 with an acoustic vortex of topological charge  $\ell = 1$  on the diffusive time scale  $\tau_{\text{diff}}^{\parallel} \approx 9.01$  s. The snapshots in Fig. 4.5(a)–(d) depict the Ficoll concentration field at several stages of the patterning process. Here, white corresponds to high concentration values and black corresponds to low concentration values. Initially, the concentration field is seen as an elongated band described by Eq. (4.1), aligned with the longitudinal axis of the chamber. Upon application of acoustics, the concentration field is rearranged into a Bessel-like pattern, manifesting the acoustic vortex. The pattern reaches its sharpest appearance in 4.5(c), before it slowly dissolves due to diffusion as seen in 4.5(d). The long diffusive time scale  $\tau_{\text{diff}}^{\parallel}$  thus sets the time scale for the existence of the pattern.

During the patterning, the concentration is maintained at the acoustic center. At the same time, away from the center, the concentration field is displaced, forming arms of Ficoll solution protruding into the water. The lengths of these arms decrease further away from the acoustic center due to the acoustic force density  $\mathbf{f}_{\text{ac}}$  radially decaying like  $(kr)^{-2}$  for  $kr \gg 1$ . The arms are formed as the result of a combined process in which the water protrudes into the Ficoll solution band at peaks of  $F_{\text{ac}}$ , while Ficoll solution protrudes into the surrounding water at valleys of  $F_{\text{ac}}$ . We can thus attribute the protrusion of the water to the acoustic-pressure term in  $F_{\text{ac}}$  and the protrusion of the Ficoll solution to the acoustic-velocity term. One might then pose the question, why do the protrusion of the solvent and the protrusion of the solute next to that look nearly equal of magnitude when the acoustic-pressure and velocity terms in  $F_{\text{ac}}$  are so unequal of magnitude as seen in Fig. 4.3(d)? This balance, I speculate, is poised by the build-up of pressure due to volume conservation, which impedes the protrusion of the water and facilitates the protrusion of Ficoll solution.

In Fig. 4.5(e), the concentration  $s_{\text{cen}}$  averaged over the height at the acoustic center (red dots in the previous panels) and the concentration  $s_{\text{cir}}$  averaged over the height and arc length along the first water protrusion (blue dashed arc) is shown vs. time. The concentration  $s_{\text{cen}}$  is constant until the pattern reaches its sharpest appearance indicated by the vertical dashed line. At the same time, the concentration  $s_{\text{cir}}$  averaged along the solvent protrusion decreases due to the solute being replaced by solvent. After the dashed line,  $s_{\text{cen}}$  decreases and  $s_{\text{cir}}$  increases due to diffusion. The difference between these two averaged concentrations is defined as the concentration contrast  $C$ ,

$$C = s_{\text{cen}} - s_{\text{cir}}. \quad (4.21)$$

which provides a measure to quantitatively study the patterning of the Ficoll solution. This contrast  $C$  is plotted vs. time in Fig. 4.5(f). The different stages of the pattern indicated on the contrast curve by the letters. The sharpest appearance of the pattern is defined as the contrast peak occurring at the characteristic time  $t_{3\text{D}}^* = 0.37\tau_{\text{diff}}^{\parallel} = 3.4$  s, hence referred to as the patterning time. Between **a** and **c**, we

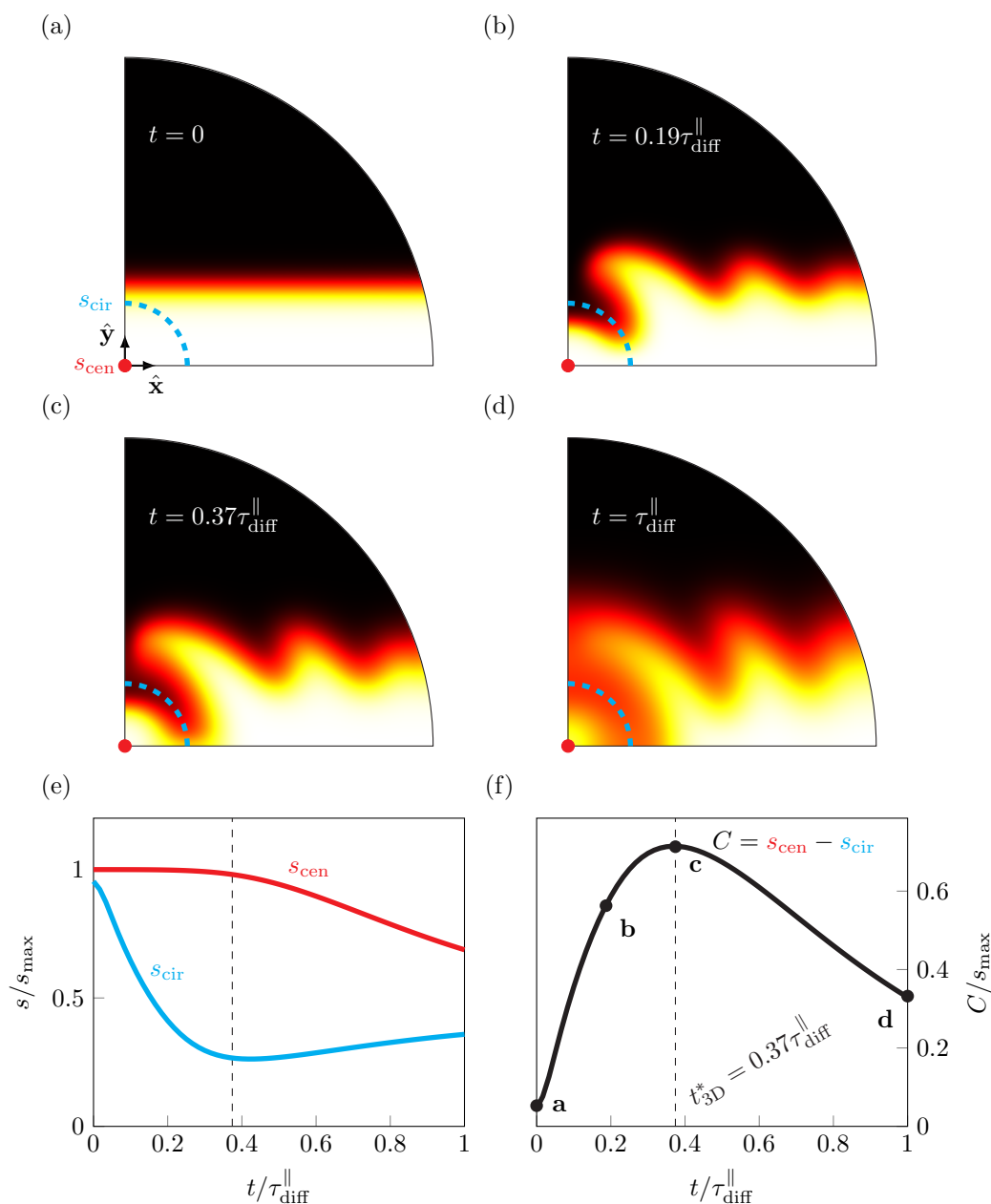


Figure 4.5: Patterning of Ficoll PM400 by an acoustic vortex of topological charge 1 on the diffusive time scale  $\tau_{\text{diff}}^{\parallel} = 9.01$  s. (a)–(d) Top-down view of temporal evolution of concentration field. White represents a high concentration, and black represents a low concentration. The acoustic center lies in origo in the bottom left corner at the red point. (e) The concentration averaged in the height at the red point (red curve), and the concentration averaged in the height and along the blue arc (blue curve). (f) The concentration contrast  $C$  vs. time. Letters label Figs. (a)–(d). The vertical dashed lines indicate the time  $t^*_{3D}$  at maximum contrast.

find the stages, in which the advective transport of the acoustics-induced flow is dominant. With this  $t^*$ , the effective Péclet number can readily be obtained as  $\tau_{\text{diff}}/t_{3\text{D}}^* \approx 1$ . Using  $t_{3\text{D}}^*$  for calculating  $Pe_{\text{eff}}$  yields the number in an averaged sense, in which it has been averaged over the time between 0 and  $t_{3\text{D}}^*$ . This  $Pe_{\text{eff}}$  would be equivalent to drawing a line directly from **a** to **c** in Fig. 4.5(f) and using the slope of this line for the velocity. Looking at the contrast curve, we find that by the time  $t = t_{3\text{D}}^*/2$ , the contrast curve is  $> 0.75$  of its maximum value. The curve rounds off after this point. Therefore, the true  $Pe_{\text{eff}}$  is greater than the calculated value, especially in the beginning of the patterning. The actual Péclet number  $Pe$  is obtained by  $\epsilon^{-1}Pe_{\text{eff}} \approx 1.6$ .

The snapshots in Figs. 4.6(a)–(d) shows the evolution of the height-averaged velocity field during patterning. It features flow rolls, which decay the further the rolls are from the acoustic center. Although the fluid should be at rest at  $t = 0$  in Fig. 4.6(a), we find a well-developed flow. The reason for this is the quasi-static assumption neglecting the inertia of the fluid. However, this does not affect the results due to inertia playing a negligible role. Figure 4.6(e) shows the maximum flow speeds of the different components (solid lines) and corresponding height-averaged flow speeds (dashed lines) calculated with Eq. (4.19). We find that the vertical velocity component,  $v_z$ , generally is low compared to the lateral velocity components. It was found that the vertical acoustic force density component,  $f_{\text{ac},z}$ , was balanced by the pressure gradient,  $\partial_z p$ . Typically, this is a result of volume conservation in shallow fluid flows. Furthermore, due to its asymmetry in the  $z$ -axis,  $v_z$  averages to zero over the height:  $\langle v_z \rangle = 0$ . In Fig. 4.6(e), we see the ratio of the maximum flow speeds and their height-averaged value. In Hele-Shaw flows, characterizing flows between narrowly spaced parallel plates, the value of this ratio is  $3/2$ . This value is indicated by the horizontal solid line. We find that the lateral velocity components,  $v_x$  and  $v_y$ , deviate from this value by 6% and 4% on average over the simulated time, as measured by the normalized  $L^2$ -norm. The flow is therefore not perfectly parabolic in the height dimension as expected of Hele-Shaw flows. This is because the relevant aspect ratio of the flow is not the geometric aspect ratio  $h/W = 0.03$ , but rather the acoustic aspect ratio  $kh = 0.62$ .

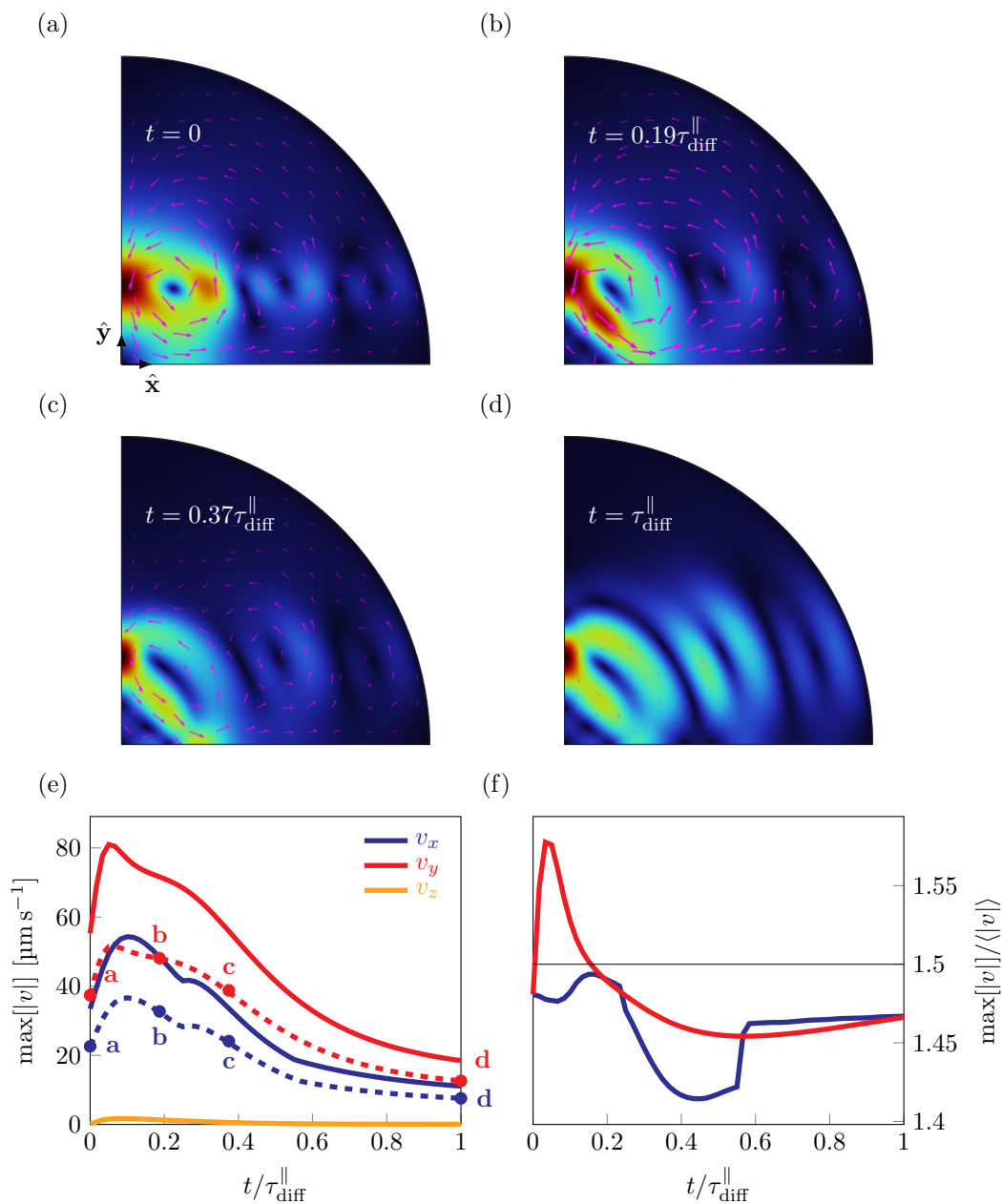


Figure 4.6: Flow field induced by the acoustic force density. (a)–(d) Evolution of the height-averaged flow field. Color indicates velocity magnitude (red = high, dark blue = low). Arrows indicate the flow direction and magnitude between (a)–(d). (e) Maximum velocity magnitude  $\max[|v|]$  vs. time. Dashed lines indicate their height-averaged values. Letters corresponds to (a)–(d). (f) The ratio of the maximum flow speeds and their height-averaged values vs. time. The horizontal solid line indicate the value  $3/2$  of Hele-Shaw flows.

## Chapter 5

# The 2D Hele-Shaw model

Performing 3D full-system simulations is often impractical due to the large number of degrees of freedom involved, leading to significant computational expenses and computing times. In the present case, such simulations are feasible, as evidenced by the previous chapter; but, the long computing times makes it necessary to explore alternative approaches. One approach is to develop an effective 2D model, whereby the number of spatial dimensions is reduced from 3 to 2.

In this chapter, we develop an effective 2D model of the 3D system presented in Chap. 4, formulated in terms of the height-averaged velocity, pressure, and Ficoll concentration. In addition to simplifying the system for the purpose of simulating it, the height-averaged model offers the advantage of aligning with experiments where the height dimension is not resolved, because observations are made through the top-down view of a microscope.

### 5.1 Long-wavelength formulation

The 2D model is formulated in terms of the height-averaged velocity, pressure, and Ficoll concentration under assumption of long acoustic wavelengths relative to chamber height. This long-wavelength assumption is expressed by the following condition on the ratio of wavelength to chamber height, defining the *acoustic aspect ratio*  $\epsilon$ :

$$\epsilon = kh = \frac{2\pi h}{\lambda} \ll 1. \quad (5.1)$$

Subject to this condition, spatial variations on the scale of the wavelength occur much slower than those on the scale of the height. This disparity leads to a simplified set of equations, permitting the solving of the equations in the height and their subsequent height-averaging defined in Eq. (4.19)

### 5.1.1 Non-dimensionalization of governing equations

We proceed to non-dimensionalize the governing equations given in Eq. (4.10). Neglecting gradients in viscosity, these equations are

$$\nabla \cdot \mathbf{v} = 0, \quad (5.2a)$$

$$0 = -\nabla p + \eta \nabla^2 \mathbf{v} + F_{\text{ac}} \nabla s, \quad (5.2b)$$

$$\partial_t s + (\mathbf{v} \cdot \nabla) s = \nabla \cdot (D \nabla s). \quad (5.2c)$$

The variables are then scaled as follows:

$$\begin{aligned} x &= \hat{x}/k, & y &= \hat{y}/k, & z &= h\hat{z}, & t &= \hat{t}/kU_0, & \rho &= \rho_w \hat{\rho}, \\ v_x &= U_0 \hat{v}_x, & v_y &= U_0 \hat{v}_y, & v_z &= \epsilon U_0 \hat{v}_z, & p &= (\eta_w U_0 / kh^2) \hat{p}, & F_{\text{ac}} &= [\kappa_w (j_1^{\text{max}} p_{\text{ac}}^{\text{max}})^2 / 4kh] \hat{F}_{\text{ac}}, \\ \eta &= \eta_w \hat{\eta}, & s &= s_{\text{max}} \hat{s}, & D &= D_w \hat{D}, & Re &= \rho_w U_0 h / \eta_w, & Pe &= U_0 h / D_w, \end{aligned} \quad (5.3)$$

in which the characteristic flow speed  $U_0$  is obtained by balancing the magnitude of the acoustic force density with that of viscous stress,

$$U_0 = (1/4) \kappa_w (j_1^{\text{max}} p_{\text{ac}}^{\text{max}})^2 s_{\text{max}} h / \eta_w \sim 800 \mu\text{m s}^{-1}.$$

The factor of  $\epsilon$  in the vertical velocity component,  $v_z$ , is a result of volume conservation.

With this scaling, the derivatives become

$$\partial_t = (\epsilon U_0 / h) \hat{\partial}_t, \quad \partial_x = (\epsilon / h) \hat{\partial}_x, \quad \partial_y = (\epsilon / h) \hat{\partial}_y, \quad \partial_z = (1/h) \hat{\partial}_z, \quad (5.4)$$

Here, the factor of  $\epsilon$  in the lateral derivatives implies that variations in these directions are very small on the scale of  $h$ . We introduce the following notation for the gradient:

$$\nabla = \nabla_{\parallel} + \hat{z} \partial_z \quad \text{with} \quad \nabla_{\parallel} \equiv \hat{x} \partial_x + \hat{y} \partial_y \sim (\epsilon / h). \quad (5.5)$$

Now, on substituting Eq. (5.3) into the Stokes equations (5.2b), the equations become

$$0 = -\hat{\partial}_x \hat{p} + \epsilon^2 \hat{\eta} \hat{\nabla}_{\parallel}^2 \hat{v}_x + \hat{\eta} \hat{\partial}_z^2 \hat{v}_x + \hat{F}_{\text{ac}} \hat{\partial}_x \hat{s}, \quad (5.6a)$$

$$0 = -\hat{\partial}_y \hat{p} + \epsilon^2 \hat{\eta} \hat{\nabla}_{\parallel}^2 \hat{v}_y + \hat{\eta} \hat{\partial}_z^2 \hat{v}_y + \hat{F}_{\text{ac}} \hat{\partial}_y \hat{s}, \quad (5.6b)$$

$$0 = -\hat{\partial}_z \hat{p} + \epsilon^4 \hat{\eta} \hat{\nabla}_{\parallel}^2 \hat{v}_z + \epsilon^2 \hat{\eta} \hat{\partial}_z^2 \hat{v}_z + \hat{F}_{\text{ac}} \hat{\partial}_z \hat{s}, \quad (5.6c)$$

In the long-wavelength limit,  $\epsilon \rightarrow 0$ , the terms containing  $\epsilon$  vanish, and the equations reduce to

$$0 = -\hat{\partial}_x \hat{p} + \hat{\eta} \hat{\partial}_z^2 \hat{v}_x + \hat{F}_{\text{ac}} \hat{\partial}_x \hat{s}, \quad (5.7a)$$

$$0 = -\hat{\partial}_y \hat{p} + \hat{\eta} \hat{\partial}_z^2 \hat{v}_y + \hat{F}_{\text{ac}} \hat{\partial}_y \hat{s}, \quad (5.7b)$$

$$0 = -\hat{\partial}_z \hat{p} + \hat{F}_{\text{ac}} \hat{\partial}_z \hat{s}, \quad (5.7c)$$

resembling the equations of 2D Hele-Shaw flows, albeit with the inclusion of acoustic force density. The last equation expresses the balance between the acoustic force density and the pressure gradient in the height, as observed in 3D simulations.

Similarly, substituting the scaled variables into the advection-diffusion equation (5.2c) yields

$$\epsilon Pe \hat{\partial}_t \hat{s} + \epsilon Pe (\hat{\mathbf{v}} \cdot \hat{\nabla}) \hat{s} = \epsilon^2 \hat{\nabla}_{\parallel} \cdot (\hat{D} \hat{\nabla}_{\parallel} \hat{s}) + \hat{\partial}_z (\hat{D} \hat{\partial}_z \hat{s}). \quad (5.8)$$

On the left-hand side of the equation, we recognize the effective Péclet number,  $Pe_{\text{eff}} = \epsilon Pe$ . To the lowest order in  $\epsilon$  and given that  $Pe_{\text{eff}} \ll 1$ , the equation  $\hat{\partial}_z (\hat{D} \hat{\partial}_z \hat{s}) = 0$  expresses that  $s$  remains in a steady state in the height at all times. Had we chosen the short diffusive time scale  $h^2/D_w$  for our characteristic time, the foregoing equation would have been  $\hat{\partial}_z (\hat{D} \hat{\partial}_z \hat{s}) = \hat{\partial}_t \hat{s}$ , leading transient behaviour on this short time scale. However, because our focus lies on the longer time scale of  $1/U_0 k$ , we do not resolve this short transient behaviour, and  $s$  only changes over time on the independent  $t_1 = (1/U_0 k) \hat{t}$  and  $t_2 = (1/D_w k^2) \hat{t}$  time scales, with the subscripts indicating orders in  $\epsilon$ . Accordingly, we omit the short time scale dynamics on  $t_0 = (h^2/D_w) \hat{t}$  altogether.

### 5.1.2 Derivation of height-averaged equations

By performing dimensional analysis of the governing equations of the system, we have determined the scaling of the different terms of the equations with respect to the small parameter  $\epsilon$ . Now we develop a simple 2D model within a perturbation framework using  $\epsilon$ . Generally, the fields are written as

$$\mathbf{v} = \mathbf{v}^{(0)} + \mathbf{v}^{(1)} + \dots, \quad p = p^{(0)} + p^{(1)} + \dots, \quad s = s^{(0)} + s^{(1)} + \dots, \quad (5.9)$$

where the superscripts indicate the orders in  $\epsilon$ . Note that  $\mathbf{v}^{(0)}$  does not contain a vertical component, resulting from volume conservation.

Intuitively, the order of each term indicates the time scale at which it arises. For example,  $s^{(0)}$  develops on the time scale  $t_0$ . Subsequently, the variation  $s^{(1)}$  emerges on  $t_1$ , followed by  $s^{(2)}$  on  $t_2$ . Each term is still a function of every other time scale. For example,  $s^{(1)}$  is still a function of  $t_0$ , although the term itself occurs on  $t_1$ . This is because  $s^{(1)}$  need to reach a steady-state in the height dimension, which occurs on  $t_0$ . However, due to the relative fast occurrence of  $t_0$  compared to  $t_1$ , the term  $s^{(1)}$  can be considered fully developed in the height at all times. Moreover, even though a higher-order term like  $s^{(1)}$  emerge later than  $s^{(0)}$ , it can still influence  $s^{(0)}$  even later. An example of this is Taylor dispersion, in which the variation  $s^{(1)}$  impacts  $s^{(0)}$  on the time scale  $t_2$ . We will explore this effect in more detail in Sec. 5.3.

When truncating the foregoing expansion, we should stop at the term that corresponds to the observed time scale of the system. In the previous chapter, we examined the contrast curve on the time scale of  $\tau_{\text{diff}}^{\parallel}$ , and so we ought to go to second order of  $s$ . Nonetheless, we keep this 2D model simple and truncate the series at zeroth-order. Later we consider the consequences of moving beyond zeroth-order. The fields,

then, are written as

$$\mathbf{v} = \mathbf{v}^{(0)}(\mathbf{r}), \quad p = p^{(0)}(\mathbf{r}), \quad s = s^{(0)}(\mathbf{r}, t), \quad (5.10)$$

neglecting the explicit time-dependency of  $\mathbf{v}$  but retain that of  $s$  on account of  $\eta_w/\rho_w D_w \sim 8 \times 10^3 \gg 1$ . Furthermore, we define

$$\eta^{(0)} \equiv \eta_w \exp(bs^{(0)}) \quad \text{and} \quad D^{(0)} \equiv D_w(1 + d_1 s^{(0)} + d_2 (s^{(0)})^2). \quad (5.11)$$

We start the analysis and height-averaging of the equations with the advection-diffusion equation. This equation turns out to be trivial to height-average to the order of  $s^{(0)}$  in  $\epsilon$ .

**The advection-diffusion equation** To zeroth order, the advection-diffusion equation reads

$$\partial_z(D^{(0)}\partial_z s^{(0)}) = 0, \quad (5.12)$$

expressing that  $s^{(0)}$  is uniform in the height at all times and therefore independent of  $z$ . Accordingly, it represents its own height-averaged quantity:

$$s^{(0)} = \langle s^{(0)} \rangle. \quad (5.13)$$

We generally make use of the above equality by always replacing  $s^{(0)}$  with its height-average.

The advection-diffusion equation to second order in  $\epsilon$  therefore is

$$\partial_t \langle s^{(0)} \rangle + (\mathbf{v}^{(0)} \cdot \nabla_{\parallel}) \langle s^{(0)} \rangle = \nabla_{\parallel} \cdot (D^{(0)} \nabla_{\parallel} \langle s^{(0)} \rangle). \quad (5.14)$$

Applying the height-average yields

$$\partial_t \langle s^{(0)} \rangle + (\langle \mathbf{v}^{(0)} \rangle \cdot \nabla_{\parallel}) \langle s^{(0)} \rangle = \nabla_{\parallel} \cdot (D^{(0)} \nabla_{\parallel} \langle s^{(0)} \rangle), \quad (5.15)$$

describing the evolution of the height-averaged concentration  $\langle s^{(0)} \rangle$  in terms of height-averaged quantities only. This concludes the height-averaging of the advection-diffusion equation.

**The Stokes equations** To zeroth-order, the Stokes equations are

$$0 = -\partial_x p^{(0)} + \eta^{(0)} \partial_z^2 v_x^{(0)} + F_{ac} \partial_x \langle s^{(0)} \rangle, \quad (5.16a)$$

$$0 = -\partial_y p^{(0)} + \eta^{(0)} \partial_z^2 v_y^{(0)} + F_{ac} \partial_y \langle s^{(0)} \rangle, \quad (5.16b)$$

$$0 = -\partial_z p^{(0)}, \quad (5.16c)$$

in which we have used that  $\partial_z p^{(0)} \propto \partial_z \langle s^{(0)} \rangle = 0$ .

To solve these equations in the height, we write the fields in terms of their height-averaged quantities and their variations,

$$\mathbf{v}^{(0)} = \langle \mathbf{v}^{(0)} \rangle [1 - \zeta(z)], \quad p^{(0)} = \langle p^{(0)} \rangle, \quad s^{(0)} = \langle s^{(0)} \rangle, \quad (5.17)$$

Here, the function  $\zeta$  represents the height-variation of the velocity, satisfying

$$\zeta(\pm h) = 1 \quad (5.18)$$

to enforce the no-slip condition on the top and bottom walls.

Introducing the decomposition (5.17) into the equations for the velocity and moving the viscous terms to the left-hand sides of the equations yields

$$\eta^{(0)} \langle v_x^{(0)} \rangle \partial_z^2 \zeta = -\partial_x \langle p^{(0)} \rangle + F_{\text{ac}} \partial_x \langle s^{(0)} \rangle, \quad (5.19a)$$

$$\eta^{(0)} \langle v_y^{(0)} \rangle \partial_z^2 \zeta = -\partial_y \langle p^{(0)} \rangle + F_{\text{ac}} \partial_y \langle s^{(0)} \rangle. \quad (5.19b)$$

in which only  $\zeta$  depends on  $z$ .

By integration of the foregoing equations and application of the no-slip condition (5.18), we obtain the standard parabolic velocity-profile of Hele-Shaw flows,

$$\zeta = -\frac{1}{2} \left[ 1 - 3 \left( \frac{z}{h} \right)^2 \right]. \quad (5.20)$$

We insert this back into the equations and height-average them to obtain

$$-\frac{12\eta^{(0)}}{(2h)^2} \langle \mathbf{v}^{(0)} \rangle = \nabla_{\parallel} \langle p^{(0)} \rangle - F_{\text{ac}} \nabla_{\parallel} \langle s^{(0)} \rangle, \quad (5.21)$$

describing the height-averaged flow velocity  $\langle \mathbf{v}^{(0)} \rangle$ . Evidently, the top and bottom chamber walls exert a viscous force density on the height-averaged flow, described by

$$\mathbf{f}_{\text{visc}}^{(0)} = -\frac{12\eta^{(0)}}{(2h)^2} \langle \mathbf{v}^{(0)} \rangle. \quad (5.22)$$

Equation (5.21) can be used to calculate the height-averaged velocity from the height-averaged pressure gradient and the height-averaged acoustic force density. We can eliminate the velocity entirely by application of the incompressibility condition,  $\nabla_{\parallel} \cdot \langle \mathbf{v}^{(0)} \rangle$ :

$$0 = \nabla_{\parallel} \cdot \left[ \frac{1}{\eta^{(0)}} \left( \nabla_{\parallel} \langle p^{(0)} \rangle - F_{\text{ac}} \nabla_{\parallel} \langle s^{(0)} \rangle \right) \right]. \quad (5.23)$$

This constitutes a major simplification in that the problem no longer involves solving for  $\langle \mathbf{v}^{(0)} \rangle$ .

The boundary condition for the pressure is derived by using the fact that the fluid cannot penetrate the outer boundary,

$$\hat{\mathbf{n}} \cdot \langle \mathbf{v}^{(0)} \rangle = 0 \quad \text{on outer boundaries.} \quad (5.24)$$

By Eq. (5.21), this condition is equivalent to

$$\hat{\mathbf{n}} \cdot \nabla_{\parallel} \langle p^{(0)} \rangle = F_{\text{ac}} \hat{\mathbf{n}} \cdot \nabla_{\parallel} \langle s^{(0)} \rangle \quad \text{on outer boundaries.} \quad (5.25)$$

However,  $\hat{\mathbf{n}} \cdot \nabla_{\parallel} \langle s^{(0)} \rangle = 0$  on the boundaries due to the no-flux condition; hence,

$$\hat{\mathbf{n}} \cdot \nabla_{\parallel} \langle p^{(0)} \rangle = 0 \quad \text{on outer boundaries.} \quad (5.26)$$

**Summary** In summary, the governing equations in the long-wavelength limit are

$$0 = \nabla_{\parallel} \cdot \left[ \frac{1}{\eta^{(0)}} \left( \nabla_{\parallel} \langle p^{(0)} \rangle - F_{\text{ac}} \nabla_{\parallel} \langle s^{(0)} \rangle \right) \right], \quad (5.27a)$$

$$\partial_t \langle s^{(0)} \rangle + \langle \mathbf{v}^{(0)} \rangle \cdot \nabla_{\parallel} \langle s^{(0)} \rangle = \nabla_{\parallel} \cdot (D^{(0)} \nabla_{\parallel} \langle s^{(0)} \rangle), \quad (5.27b)$$

in which  $\langle \mathbf{v}^{(0)} \rangle$  is calculated using

$$\langle \mathbf{v}^{(0)} \rangle = -\frac{(2h)^2}{12\eta^{(0)}} \left( \nabla_{\parallel} \langle p^{(0)} \rangle - F_{\text{ac}} \nabla_{\parallel} \langle s^{(0)} \rangle \right), \quad (5.28)$$

and the boundary conditions are

$$\hat{\mathbf{n}} \cdot \nabla_{\parallel} \langle p^{(0)} \rangle = 0, \quad (5.29a)$$

$$\hat{\mathbf{n}} \cdot \nabla_{\parallel} \langle s^{(0)} \rangle = 0. \quad (5.29b)$$

## 5.2 Results and discussion

First, we inspect the assumption of a parabolic velocity profile. Figure 5.1 compares the velocity profile of the 3D simulation with the parabolic profile of Hele-Shaw flow at  $\epsilon = 0.62$ . In Fig. 5.1(a), the velocity in the  $xy$ -plane at  $z = 0$  is shown at time  $t = 0.72\tau_{\text{diff}}^{\parallel}$ . The velocity field has been evaluated at the magenta point along the height  $z = [0, h]$  and shown in Fig. 5.1(b) at  $t = 0.72\tau_{\text{diff}}^{\parallel}$ , the time at which the discrepancy is greatest between the 3D simulation and the assumed parabola. The reason for choosing this point is that it lies on the arc, along which we calculate the concentration contrast. The figure shows good agreement between the simulated velocity profile and the analytical parabolic profile at the magenta point with a discrepancy of only 2%. However, this discrepancy reaches 5% at the region of the great flow speeds (dark red region) seen in Fig. 5.1(a). The discrepancy at the magenta point is plotted against time in Fig. 5.1(c). It fluctuates in the beginning, but eventually finds a stable level. In the best case, these fluctuations are physics-related; in the worst case, they are numerics-related. Based on the numerical tests, I do have faith in the simulation results, so I work with the hypothesis that they are physical. Figure 5.1(d) shows the relative difference between the simulated velocity profile and the analytical profile calculated by  $\int (u - u_{\text{ref}}) dz / \int u_{\text{ref}} dz$ . Foremost, these curves are more smooth, which does not out-rule physics as source of the discrepancy. We find that the  $y$ -component experience a negative dip peaking at  $t = 0.13\tau_{\text{diff}}^{\parallel}$ , suggesting an increased flow resistance relative to that of the parabolic profile. At later times, this difference becomes positive, suggesting a decreased flow resistance. My hypothesis is that the viscous resistance generally is smaller because  $\epsilon$  is large, and the increased flow resistance in the beginning is caused by viscous height-variation, resulting from the solute concentration

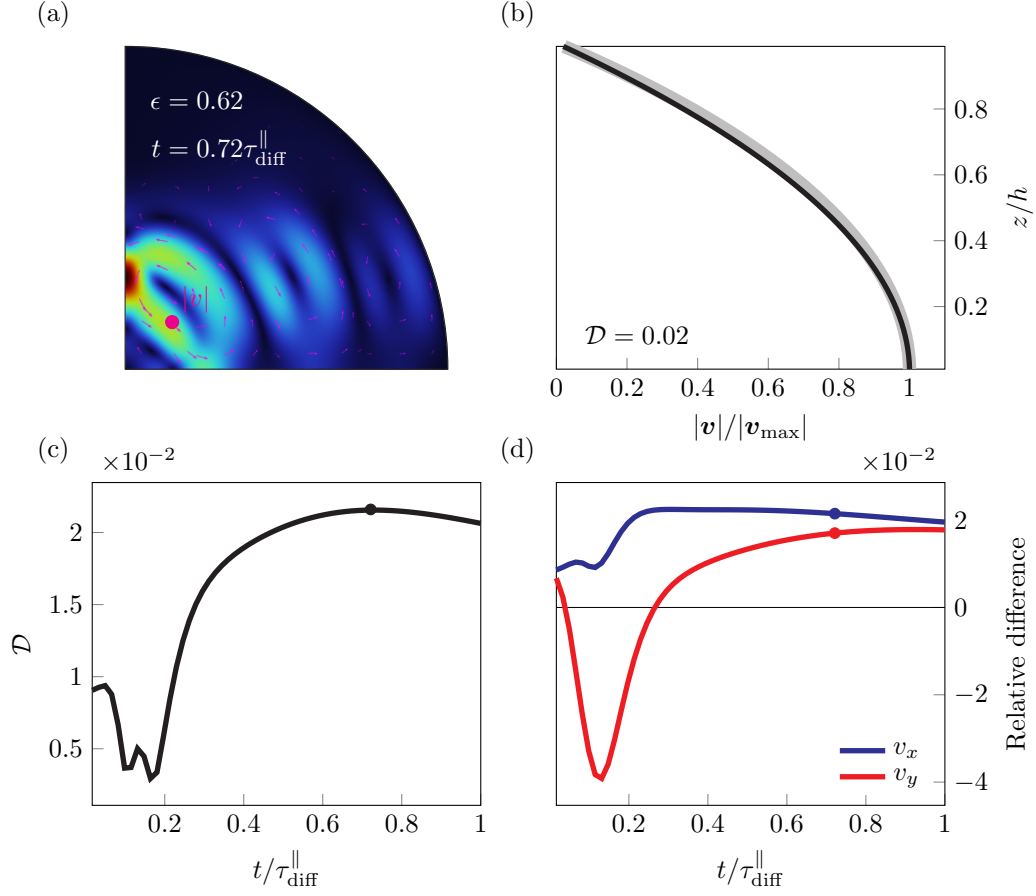


Figure 5.1: The 3D velocity profile. (a) Snapshot of the 3D velocity field viewed in the  $xy$ -plane at  $t = 0.72\tau_{\text{diff}}^{\parallel}$ . The velocity magnitude is greatest at red and lowest at dark blue. (b) The 3D velocity profile (gray) evaluated at the magenta point in (a) and compared to the parabolic profile of Hele-Shaw flow. (c) The discrepancy between the 3D velocity profile and the parabolic profile evaluated in the magenta point in (a). The discrepancy is largest at  $t = 0.72\tau_{\text{diff}}^{\parallel}$  at this point. (d) The relative difference in the height calculated by  $\int (u - u_{\text{ref}}) dz / \int u_{\text{ref}} dz$ , with  $u$  being the field and  $u_{\text{ref}}$  the reference.

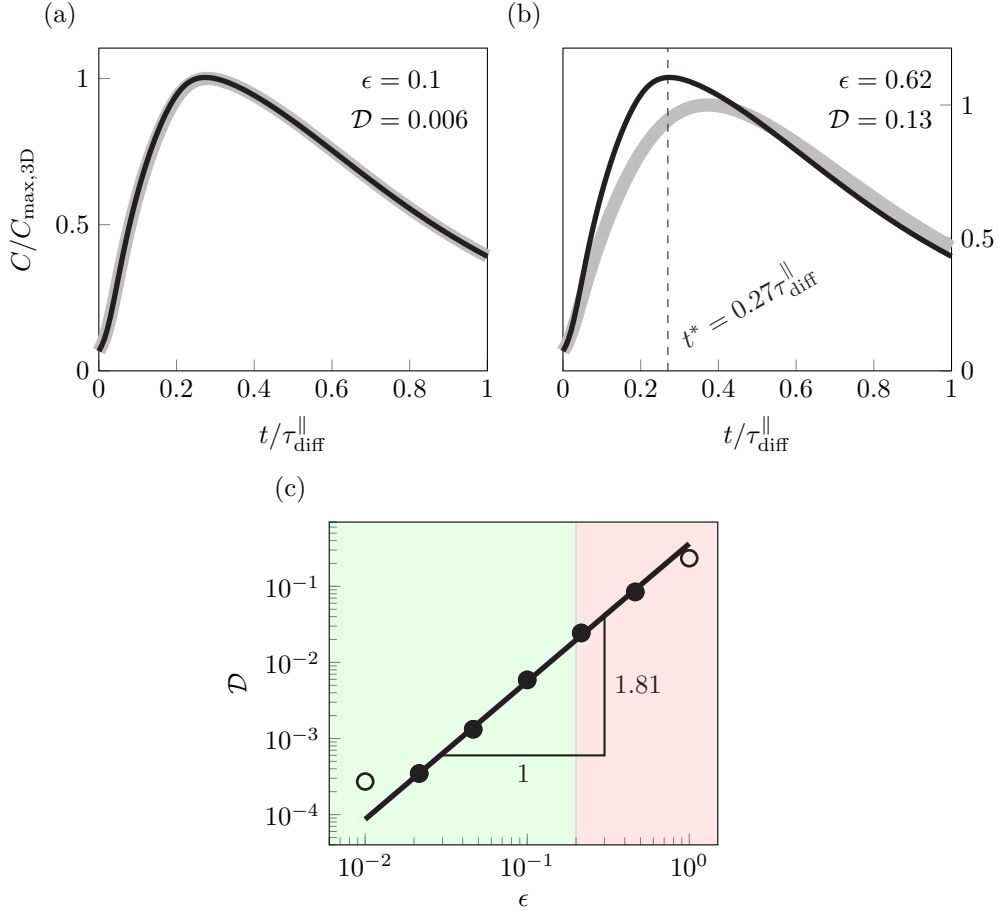


Figure 5.2: Contrast curves of the 2D Hele-Shaw model (black) and 3D model (light gray) for (a)  $\epsilon = 0.1$  and (b)  $\epsilon = 0.62$ . (c) Relative difference  $\mathcal{D}$  between the models vs.  $\epsilon$ ; green shading indicates perturbative regime and red shading non-perturbative regime; line is fitted to solid points. Acoustic pressure amplitude was scaled with  $\epsilon^{-2}$  relative to 0.19 MPa at  $\epsilon = 0.62$ .

varying in height.

Figure 5.2 compares the contrast curves obtained by the 2D Hele-Shaw model and the full 3D model for several values of  $\epsilon$ . As seen in Fig. 5.2(a), the two models show great agreement in the long-wavelength regime,  $\epsilon \ll 1$ , even for the relatively large value of  $\epsilon = 0.1$ . The curve obtained by the 2D model (black) lies directly on top of the curve obtained by the 3D model (gray). Measuring the discrepancy  $\mathcal{D}$  between the models by the normalized  $L^2$ -norm difference, it comes out at  $\mathcal{D} = 0.006$ , i.e., less than 1%. The patterning process is therefore described well by the simple Hele-Shaw flow model for long wavelengths compared to the chamber height.

Increasing  $\epsilon$  to the experimental value of 0.62, the 2D model no longer describes the contrast curve very well. Figure 5.2(b) shows this contrast curve compared with that of the 3D model; the error is  $\mathcal{D} = 0.13$ . The two curves are misaligned around the peak, occurring earlier ( $0.73$  of  $t_{3D}^*$ ) and peaking

higher (1.10 of  $C_{\max,3D}$ ) in the 2D model than in the 3D model. The discrepancies of the quantities  $t^*$  and  $C_{\max}$  are related, since the faster the pattern is formed, the less time diffusion has to lower the contrast before the contrast peaking. The flow velocity is generally larger in the 2D model than the 3D model, leading to these discrepancies. The subsequent diffusive decay is affected by the misalignment, but the rates of decay between the two models appears to agree. Regardless, the concentration fields and contrast curves are qualitatively identical between the models. The 2D model formulated under the assumption of  $\epsilon \ll 1$  describes the patterning decently despite  $\epsilon = 0.62$ , which is considered very large. The 2D simulation was completed in 5 minutes, involving 37,529 degrees of freedom with quartic basis functions for the solute concentration field  $s$  and cubic for the pressure field  $p$ . The higher order of basis functions was necessary due to the greater flow speeds of the 2D model and consequently greater  $Pe_{\text{cell}}$ . The runtime of 5 minutes is significantly shorter than the 3 hours of the 3D simulation. Going from 3D to 2D does not address the problem of high Péclet numbers  $Pe$  directly. For moderately high  $Pe \sim 10$ , the 2D simulation also took hours to complete, but these simulations would not have been possible to perform in 3D.

Two candidates for the explaining the misalignment at high  $\epsilon$  are foremost the viscous shear stresses in lateral dimensions,  $\eta \nabla_{\parallel}^2 \mathbf{v}$ , and the height variation of the concentration field—both of which are neglected under the long-wavelength assumption. The consequence of neglecting the former is that the 2D model generally predicts higher flow speeds than the 3D model. We return to this in the next chapter. The latter leads to Taylor dispersion, which describes the enhanced diffusion of a slowly diffusing solute in the direction of the flow. This additional diffusion scales with the Péclet number squared [23, 24]:  $KPe^2$ , in which  $K$  is dimensionless coefficient that depends on the flow profile and hence the geometry. The scaling with  $Pe^2$  implies that the enhanced diffusion is significant for slowly diffusing particles like those of Ficoll PM400 solutions. For Hele-Shaw flow,  $K = 2/105$  [25] and with the Péclet number  $Pe = \epsilon^{-1} \tau_{\text{diff}}/t^* = 2.3$  of our 2D model, the relative additional diffusion is  $KPe^2 = 0.1$ , i.e., the diffusion occurs at 1.1 times the normal rate. Remembering that  $\epsilon^{-1} \tau_{\text{diff}}/t^*$  generally underestimates  $Pe$ , dispersion can be even more prominent than expected from the previous calculation, and we got evidence to suspect that dispersion can play a role in the discrepancy between the 2D model and the 3D model. In the next section, a model for Taylor dispersion is formulated and tested.

Figure 5.2(c) shows the convergence of the 2D model to the 3D model in the perturbation parameter  $\epsilon$ . The convergence is quantified by the discrepancy  $\mathcal{D}$  between the curves of the two models, calculated using the normalized  $L^2$ -norm defined in Eq. (3.16). The parameter  $\epsilon$  is varied by changing the height  $h$ . To compensate for the increased flow resistance of reducing  $h$ , the acoustic force density is scaled accordingly by  $\epsilon^{-1}$ . Between  $\epsilon = 0.01$  and  $\epsilon = 1$ , the discrepancy exponentially increases like  $\sim \epsilon^{1.81}$ , which has been obtained by fitting a linear function to the data on the log scale. The expectation was that the exponent would be  $\approx 2$ , since Taylor dispersion and the lateral viscous shear stresses enter the governing equations to second order in  $\epsilon$ . There can be several reasons for this not being the case. One is that the Péclet number  $Pe$  is also affected by varying  $h$  to vary  $\epsilon$ . For decreasing  $h$  and thus  $\epsilon$ , this leads to faster convergence because  $Pe$  becomes smaller on top of  $\epsilon$  becoming smaller. Another is the viscosity variation in the height, which we have not addressed yet. There is also the boundary conditions for the

velocity field, which is a no-slip condition in the 3D model, and a no-flux condition in the 2D Hele-Shaw model due to the absence of lateral viscous terms. This error should have been minimized by  $R$  fulfilling  $F_{ac}(kR) = 0$  and the concentration contrast being evaluated relatively far from this boundary.

For the fit, the outermost points on the  $\epsilon$ -interval has been left out due to their misalignment with the remaining points that exhibit convincing exponential convergence. The argument for disregarding the point in  $\epsilon = 1$  is that this  $\epsilon$  is far out of the perturbative regime of the model. Here, we cannot expect  $\mathcal{D} \sim \epsilon^2$  to hold, because the separation of the equations into orders of  $\epsilon$  does not make sense for this large  $\epsilon$ . As for the point in  $\epsilon = 0.01$ , the discrepancy is so small ( $< 0.001$ ) that errors from other sources might be dominant. From the mesh refinement study, we know the errors associated with the mesh itself is on order of  $10^{-3}$ . The exponential convergence in  $\epsilon$  in Fig. 5.2(c) holds until the errors become this small, suggesting the mesh become the dominant source of errors.

## 5.3 Dispersion

We now consider the consequences of dispersion for the patterning process. We are going to develop a model for dispersion, which is based off of Sir Taylor's procedure in his original paper [23]. In our model for dispersion, however, we permit the imposing flow field to vary streamwise, and the physical parameters depend on the local concentration of Ficoll PM400.

The underlying assumption enabling this analysis is that the velocity is slowly varying in the lateral directions. This incidentally corresponds to the condition  $\epsilon \ll 1$ . Consequently, the analysis carried out in Sec. 5.1.2 is in line with that of Taylor, with  $s^{(1)}$  in Eq. (5.9) corresponding to the small height-variation generating dispersion.

### 5.3.1 Dispersion model

We write

$$s(\mathbf{r}, t_1, t_2) = s^{(0)} + s^{(1)} + s^{(2)}, \quad (5.30)$$

going to second order to eventually show that this does not affect  $\langle s^{(0)} \rangle$  on the long diffusive time scale,  $t_2$ .

Including  $s^{(1)}$ , the first-order advection-diffusion equation is

$$\partial_{t_1} \langle s^{(0)} \rangle + (1 - \zeta) \langle \mathbf{v}^{(0)} \cdot \nabla_{\parallel} \rangle \langle s^{(0)} \rangle = \partial_z (D^{(0)} \partial_z s^{(1)}), \quad (5.31)$$

in which we have used that  $s^{(0)} = \langle s^{(0)} \rangle$  and  $\mathbf{v}^{(0)} = \langle \mathbf{v}^{(0)} \rangle [1 - \zeta(z)]$ . To obtain an equation describing  $s^{(1)}$ , we apply the height-average to this equation and use the no-flux condition  $\langle \partial_z (D^{(0)} \partial_z s^{(1)}) \rangle = 0$ , resulting in

$$\partial_{t_1} \langle s^{(0)} \rangle + \langle \mathbf{v}^{(0)} \cdot \nabla_{\parallel} \rangle \langle s^{(0)} \rangle = 0, \quad (5.32)$$

Then, subtracting this mean equation from the first-order equation yields

$$-\zeta(\langle \mathbf{v}^{(0)} \rangle \cdot \nabla_{\parallel}) \langle s^{(0)} \rangle = \partial_z(D^{(0)} \partial_z s^{(1)}), \quad (5.33)$$

Through  $\zeta$ , this equation expresses that  $s^{(1)}$  is produced by the variation of velocity over the height of the chamber. Furthermore, we note that the left-hand side averages to zero over the height due to  $\langle \zeta \rangle = 0$ . This means that the height-average of  $s^{(1)}$  itself must vanish:

$$\langle s^{(1)} \rangle = 0. \quad (5.34)$$

The equation for  $s^{(1)}$  is given by (5.33) with  $\zeta$  substituted from Eq. (5.20). Integrating this equation and applying the conditions for no-flux and vanishing height-average then leads to the solution

$$s^{(1)} = -\frac{h^2}{4D^{(0)}} (\langle \mathbf{v}^{(0)} \rangle \cdot \nabla_{\parallel}) \langle s^{(0)} \rangle \left[ \frac{7}{30} - \left(\frac{z}{h}\right)^2 + \frac{1}{2} \left(\frac{z}{h}\right)^4 \right], \quad (5.35)$$

representing the variation of the concentration of Ficoll over the height of the chamber, resulting from variation of the velocity. When the flow occurs from a region of lower Ficoll concentration to a region of higher Ficoll concentration, the concentration of Ficoll is lower toward the center of the flow and higher toward the top and bottom walls compared to its average value.

To second order in  $\epsilon$ , the advection-diffusion equation is

$$\partial_{t_1} s^{(1)} + \partial_{t_2} \langle s^{(0)} \rangle + (1 - \zeta)(\langle \mathbf{v}^{(0)} \rangle \cdot \nabla_{\parallel}) s^{(1)} = \nabla_{\parallel} \cdot (D^{(0)} \nabla_{\parallel} \langle s^{(0)} \rangle) + \partial_z(D^{(0)} \partial_z s^{(2)}) \quad (5.36)$$

Applying the height-average and using  $\langle s^{(1)} \rangle = 0$  yields

$$\partial_{t_2} \langle s^{(0)} \rangle - (\langle \mathbf{v}^{(0)} \rangle \cdot \nabla_{\parallel}) \langle s^{(1)} \zeta \rangle = \nabla_{\parallel} \cdot (D^{(0)} \nabla_{\parallel} \langle s^{(0)} \rangle) \quad (5.37)$$

We see that  $s^{(2)}$  vanishes from the height-averaged equation on  $t_2$  due to the no-flux condition. Therefore, it does not influence  $\langle s^{(0)} \rangle$  on the time scale  $t_2$ , as promised. The second term on the left-hand is responsible for Taylor dispersion, which occurs on  $t_2$ . This dispersion is evaluated as

$$\langle s^{(1)} \zeta \rangle = \frac{2h^2}{105D^{(0)}} (\langle \mathbf{v}^{(0)} \rangle \cdot \nabla_{\parallel}) \langle s^{(0)} \rangle. \quad (5.38)$$

whereby the second-order equation becomes

$$\partial_t \langle s^{(0)} \rangle + (\langle \mathbf{v}^{(0)} \rangle \cdot \nabla_{\parallel}) \langle s^{(0)} \rangle = \nabla_{\parallel} \cdot (D^{(0)} \cdot \nabla_{\parallel} \langle s^{(0)} \rangle), \quad (5.39)$$

with the dispersion tensor  $D^{(0)}$  given by

$$D^{(0)} = D^{(0)} \mathbf{I} + \frac{2h^2}{105D^{(0)}} \langle \mathbf{v}^{(0)} \rangle \langle \mathbf{v}^{(0)} \rangle, \quad (5.40)$$

following some algebra. The notation  $\langle \mathbf{v}^{(0)} \rangle \langle \mathbf{v}^{(0)} \rangle$  represents the outer product of the height-averaged velocity field. The first term corresponds to diffusion, whereas the second term corresponds to dispersion. The dispersive term scales by  $(2/105)Pe^2$ , where  $2/105$  is the phenomenological coefficient of Hele-Shaw flows. Remember that  $D^{(0)}$  is a function of  $\langle s^{(0)} \rangle$ , and  $\langle \mathbf{v}^{(0)} \rangle$  can vary slowly in the lateral dimensions.

### 5.3.2 Results and discussion

Figure 5.3 compares the contrast curves obtained with the 2D Hele-Shaw models with and without dispersion for  $\epsilon = 0.62$ . In 5.3(a), we see the contrast curves together with that of the 3D model. Here, the 2D model with dispersion shows better agreement with the 3D model in the maximum contrast  $C_{\max}$  than the 2D model without dispersion. The enhanced diffusion of dispersion brought the relative difference of  $C_{\max}$  between the 2D models and the 3D model down from 10% without dispersion to 3% with dispersion. The patterning time  $t^*$ , however, is mostly unchanged, as evident by the contrast peaks of the 2D models almost aligning in time. For the two Hele-Shaw models, the patterning times are  $t^* = 0.3\tau_{\text{diff}}^{\parallel}$  with dispersion and  $t^* = 0.27\tau_{\text{diff}}^{\parallel}$  without dispersion, whereas the time is  $0.37\tau_{\text{diff}}^{\parallel}$  for the 3D model. This means the flow velocity is mostly unchanged by the dispersion. Although dispersion acts as enhanced diffusion along the flow axis, leading to faster flattening of the concentration gradient, which should result in a decreased flow, we do not observe a significant impact in practice. In 5.3(b), we see that dispersion influences the averaged concentration  $s_{\text{cir}}$ , but leaves the concentration  $s_{\text{cen}}$  at the acoustic center unchanged. This is expected, because dispersion results from advective transport, but the Ficoll at the acoustic center is not transported anywhere. The convergence of the two 2D models to the 3D model vs.  $\epsilon$  is shown in Fig. 5.3(c). As expected, the model with dispersion consistently performs better than the model without dispersion. However, the two lines representing the fits to the data points of each model eventually meet; the slope of the model without dispersion ( $= 1.81$ ) is slightly steeper than the one with dispersion ( $= 1.71$ ). This is partly explained by the Péclet number decreasing, leading to less dispersion. As  $Pe \rightarrow 0$ , dispersion becomes less effective and the two models converge to the same solution. On the other hand, we would expect the model to convergence faster (steeper slope) by increasing the complexity, if  $Pe$  is maintained at a constant value.

The influence of dispersion is more closely examined in Fig. 5.4. An image of the Ficoll solution concentration at  $t = 0.37\tau_{\text{diff}}^{\parallel}$  is shown in 5.4(a). A light blue arc between three points (a, b, c) is drawn in the first clearance of Ficoll solution in the pattern. In 5.4(b), the concentration fields obtained by the 2D model with (dashed lines) and without dispersion (solid lines) are evaluated along the light blue arc at different times during the patterning process. At  $t = 0$ , the lines are identical between the two models. At  $t = 0.14\tau_{\text{diff}}^{\parallel}$ , which is around halfway through the patterning process, it is observed that the concentration field is more flattened with dispersion than without dispersion. The enhanced diffusion from dispersion causes that more Ficoll is left behind the flow front. This leads to the lower concentration contrast of the model with dispersion. We also see that the flow fronts mostly follow along between the two 2D models. This means the velocity is mostly unchanged, despite the less pronounced gradient at the water-Ficoll solution interface. Therefore, the observed difference between the contrast curves of the 2D models is mostly caused by the enhanced diffusion of the Ficoll solution. In Fig. 5.4(c), the

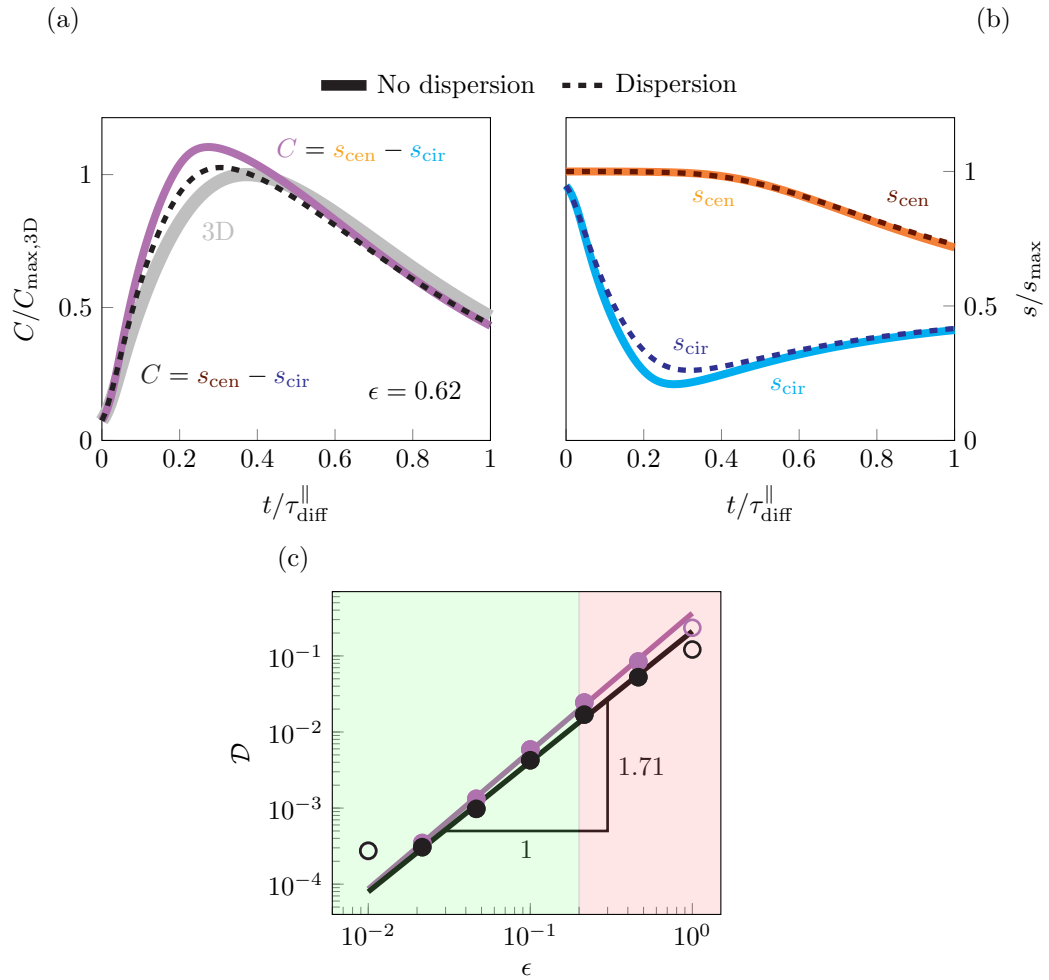


Figure 5.3: Comparison of 2D Hele-Shaw models with dispersion (dashed, black) and without dispersion (solid, violet). (a) Contrast curves obtained with the 2D models and the 3D model (light gray) for  $\epsilon = 0.62$ . (b) Concentration evaluated at the acoustic center (orange curves) and the average concentration along the first node in the concentration (blue) of the 2D models. (c) Relative difference  $\mathcal{D}$  between the 2D models and the 3D model, measured by the normalized  $L^2$ -norm. Green shading indicates the perturbative regime, while red shading represents the non-perturbative regime. Line is fitted to solid points.

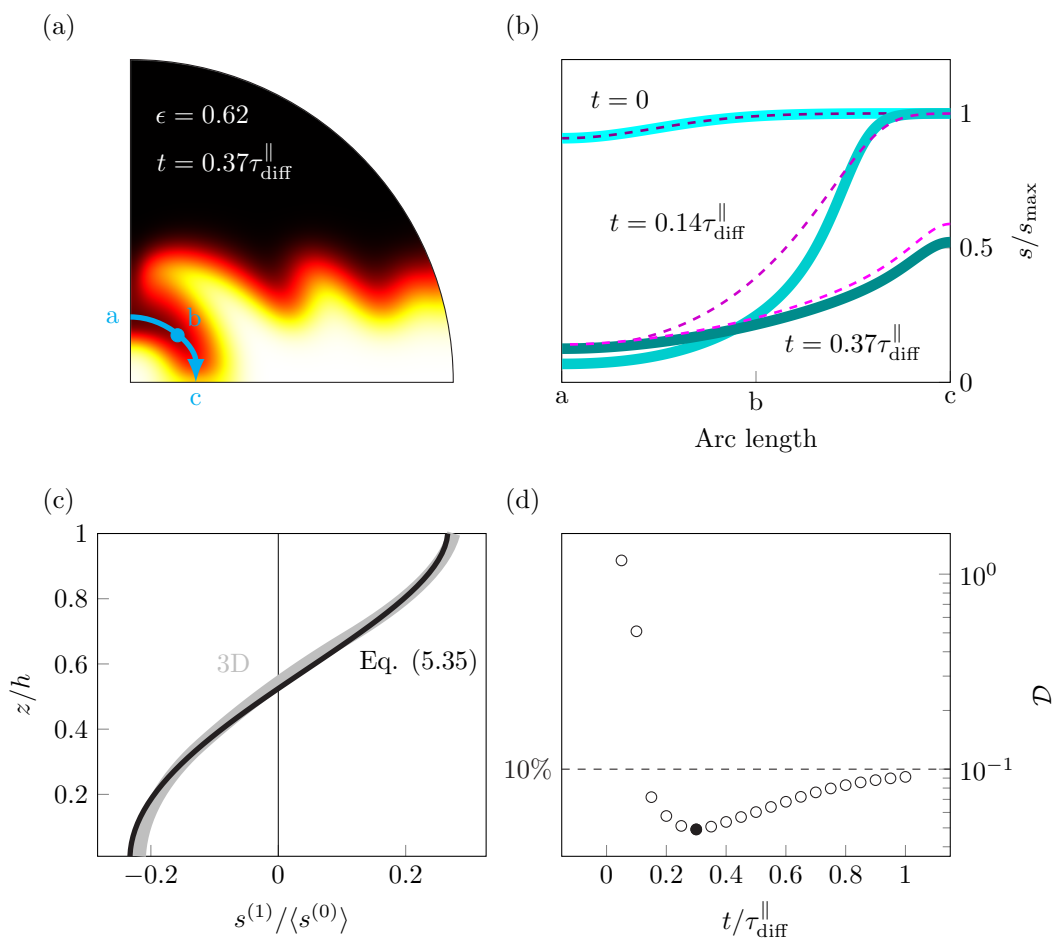


Figure 5.4: Influence of dispersion on local Ficoll concentration. (a) Snapshot of the Ficoll concentration field at  $t = 0.37\tau_{\text{diff}}^{\parallel}$  for  $\epsilon = 0.62$ . (b) The concentration field evaluated along blue arc between a, b and c at different times. Dashed lines include dispersion; solid lines do not include dispersion. (c) The expression of the height variation  $s^{(1)}$  given in Eq. (5.35) plotted together with the simulated fluctuation at  $t = 0.37\tau_{\text{diff}}^{\parallel}$  for  $\epsilon = 0.62$ . (d) The difference between the expression (5.35) and the simulated variation at different times, measured by the normalized  $L^2$ -norm. Dashed line indicate the 10% line.

theoretical profile of  $s^{(1)}$  given by Eq. (5.35) (dark blue line) is compared with the profile obtained by the 3D simulation (light gray line). This is evaluated at point b along the blue arc in 5.4(a) at the time  $t = 0.3\tau_{\text{diff}}^{\parallel}$ . Here, the negative sign of  $s^{(1)}$  below  $z/h = 0.5$  indicate that the Ficoll solution is more dilute, relative to its height-averaged concentration, towards the center than at the top and bottom walls. This is because, at the point b, pure water is being transported into the Ficoll solution. Had we evaluated  $s^{(1)}$  along one of the protrusions going out into pure water instead, then  $s^{(1)}$  had been positive near the center and negative at the top and bottom walls. The amplitude of the variations is approximately 0.2 of the height-averaged value, although it got bigger ( $\approx 0.35$ ) at earlier times. The analytical profile still manages to describe the variation of the Ficoll solution in the  $z$ -axis fairly well.

The discrepancy  $\mathcal{D}$  between the theoretical height-variation  $s^{(1)}$  and the numerical height-variation has been evaluated at point b at different times and plotted in Fig. 5.4(d). In this, the solid point indicates the point corresponding to the curve in Fig. 5.4(c). Initially, the error is quite large, but it quickly becomes smaller than 10%, where it stays for the remaining time. It is likely that the error observed in the beginning is due to the height-variation not being fully developed in the 3D model. In formulating the dispersion model, we assume that there is a considerable separation between the short diffusive time scale  $t_0$ , on which the height-variation develops in the  $z$ -axis, and the longer translational time scale  $t_1$ , on which it emerges in the lateral directions:  $Pe_{\text{eff}} \ll 1$ . This assumption corresponds to the height-profile being fully developed at all times on  $t_1 \sim \tau_{\text{adv}}$ . However, at the experimental value  $\epsilon = 0.62$  and the calculated  $Pe_{\text{eff}} \approx 1.4$ , there is not this large separation of time scales, and the assumption of a fully developed profile in the  $z$ -axis in the beginning fails. Therefore, Eq. (5.35) does not apply at these early times.

For later times after the error reaches its minimum value, the error increases and slowly flattens out around the 10%-point. It is not possible to say what the reason is with certainty. However, the exponential decay-like increase on the long diffusive time scale  $t_2 \sim \tau_{\text{diff}}^{\parallel}$  suggests that it is the inevitable lateral diffusion of  $s^{(1)}$ , represented by  $\nabla_{\parallel} \cdot (D^{(0)} \nabla_{\parallel} s^{(1)})$ . In deriving  $s^{(1)}$ , this term arising to third order in  $\epsilon$  is neglected on account of its smallness.



## Chapter 6

# The improved 2D Hele-Shaw model

In the preceding chapter, we have studied the consequences of modeling the patterning by a 2D Hele-Shaw flow, in which the lateral gradients of the velocity are neglected, leading to a simple mathematical description of the flow. In this chapter, we improve the model by adding these lateral gradients giving rise to viscous shearing in the lateral directions. This model is compared with the 3D model in Sec. 6.2 and subsequently used to explore in Sec. 6.3.

### 6.1 Improved 2D model formulation

In this improved 2D model, we simply add the lateral viscous stresses to  $\mathbf{v}^{(0)}$  while retaining the parabolic height-profile of the velocity. However, it is important to note that the parabolic profile is not correct, and the viscous body force (5.22) representing the flow resistance from the top and the bottom chamber walls should rather be written using a dimensionless parameter  $\phi(\epsilon)$ ,

$$\mathbf{f}_{\text{visc}}^{(0)} = -\frac{\phi\eta^{(0)}}{(2h)^2}\langle\mathbf{v}^{(0)}\rangle. \quad (6.1)$$

With how much the flow varies within the chamber, it is not certain that  $\phi$  remains constant throughout all regions of space, especially near the acoustic center. However, it is certain that in the long-wavelength limit,  $\epsilon \rightarrow 0$ ,  $\phi$  must approach the value 12 of Hele-Shaw flows. It likely is this  $\epsilon$ -dependency of  $\phi$  that causes the discrepancy of the velocity magnitude to the height-averaged velocity on around 2% at long times in Fig. 4.6(f). Nonetheless, we take  $\phi = 12$ , because it is our best estimate of this parameter, and it apparently is accurate within a few percent.

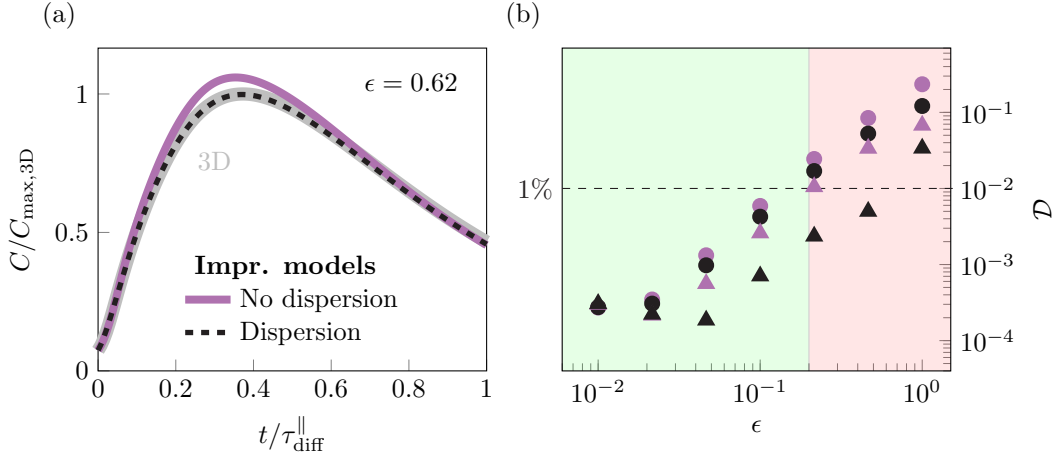


Figure 6.1: Comparison of improved 2D models with dispersion (dashed) and without dispersion (solid). (a) Contrast curves for the 2D models and the 3D model (light gray) for  $\epsilon = 0.62$ . (c) Relative difference  $\mathcal{D}$  between the 2D models and the 3D model, measured by the normalized  $L^2$ -norm. Circular points represent the 2D Hele-Shaw models of the previous chapter, and triangular points represent the improved 2D models of the present chapter. Green shading indicates perturbative regime, and red shading indicates non-perturbative regime. Dashed line indicate the 1% error threshold.

The resulting equations are

$$\nabla_{\parallel} \cdot \langle \mathbf{v}^{(0)} \rangle = 0, \quad (6.2a)$$

$$-\eta^{(0)} \nabla_{\parallel}^2 \langle \mathbf{v}^{(0)} \rangle + \frac{12\eta^{(0)}}{(2h)^2} \langle \mathbf{v}^{(0)} \rangle = \nabla_{\parallel} \langle p^{(0)} \rangle - F_{ac} \nabla_{\parallel} \langle s^{(0)} \rangle, \quad (6.2b)$$

$$\partial_t \langle s^{(0)} \rangle + (\langle \mathbf{v}^{(0)} \rangle \cdot \nabla_{\parallel}) \langle s^{(0)} \rangle = \nabla_{\parallel} \cdot (\mathbf{D}^{(0)} \cdot \nabla_{\parallel} \langle s^{(0)} \rangle), \quad (6.2c)$$

in which dispersion is included. A model without dispersion has also been studied. Results of both models are discussed for comparison in the following section.

## 6.2 Results and discussion of contrast curves

Figure 6.1(a) shows the concentration contrast obtained by the improved 2D models with and without dispersion for  $\epsilon = 0.62$ . Notably, the improved model with dispersion describes the contrast curve of the 3D model with impressive accuracy, exhibiting an discrepancy of merely  $\mathcal{D} = 0.009$ . This error being below 1% is quite astonishing, considering that the error associated with assuming the parabolic height-profile of the velocity is around 5% at  $\epsilon = 0.63$ . We would therefore expect the error of the model to be somewhere this error of the height-profile at least. The reason behind the model achieving an error below 1% remains inconclusive at this time.

Including the lateral viscous stresses improved the calculated patterning time  $t^*$  by reducing the

relative difference from 27% of the simplest 2D model to 2% of the improved model without dispersion. Then, by adding the dispersion on top of this, the relative difference of  $C_{\max}$  between the 2D model and the 3D model is reduced from 6% to 0.2%. Hence, the patterning time  $t^*$  is mostly governed by the viscosity, whereas  $C_{\max}$  is mostly governed by dispersion.

Figure 6.1(b) compares all iterations of the 2D model at different  $\epsilon$ , plotting the discrepancies between the models and the 3D model vs.  $\epsilon$ . The circular points represent the Hele-Shaw models from the previous chapter, while the triangular points represent the improved 2D models of the present chapter. The color indicates whether dispersion is included (black) or not (violet). The discrepancies consistently decrease with increasing complexity of the model; the simple 2D Hele-Shaw model (circular, violet) exhibits the largest discrepancy, followed by the same model with dispersion (circular, black). The improved 2D model with lateral viscous stresses (triangular, violet) reduces the discrepancy further, and finally, the improved 2D model with dispersion (triangular, black) attains the smallest discrepancy with the 3D model. At  $\epsilon = 0.01$ , the discrepancies are the same for all the models, likely attributed to the mesh becoming the dominant source of error.

Both lateral viscous stresses and dispersion occur to second order in  $\epsilon$  of their respective equations. However, as observed in Fig. 6.1(b), the errors associated with the model including the lateral viscous stresses (triangular, violet) consistently remain smaller than those of the model including dispersion (circular, black). This suggests that the influence of the lateral viscous stresses is more significant than that of dispersion. A possible explanation for this discrepancy is that the viscous time scale associated with these stresses,  $\tau_{\text{visc}}^{\parallel} = \rho_w / \eta_w k^2$ , is much shorter than the diffusive time scale of dispersion,  $\tau_{\text{disp}}^{\parallel} = \tau_{\text{diff}}^{\parallel} / Pe^2$ . Using  $Pe = \tau_{\text{diff}}^{\parallel} / t_{3D}^* \gtrsim 1$ , we find that their ratio is  $\tau_{\text{disp}}^{\parallel} / \tau_{\text{visc}}^{\parallel} = (\eta_w / D_w \rho_w) / Pe^2 \lesssim 8000$ . Hence, we are going to observe the consequences of the lateral viscous stresses before those of dispersion. This observation is consistent with the fact that the model with lateral viscous stresses and no dispersion describes the contrast curve of the 3D model better than the model with dispersion and no lateral viscous stresses at early times. The contrast curve of the former does not depart significantly from the 3D model until  $t \sim 0.1\tau_{\text{diff}}^{\parallel}$  [see Fig. 6.1(a)], whereas the latter begins to deviate from the 3D model right at the beginning [see Fig. 5.3(a)].

## 6.3 Exploring parameter space

We have formulated a 2D model with the height-averaged fields in the long-wavelength limit,  $\epsilon \ll 1$ , and tested it against a 3D model at  $\epsilon = 0.62$ , which yielded positive results. The 2D model is comprised of the equations in Eq. (6.2), describing a Hele-Shaw flow including lateral viscous gradients and dispersion. We can now simulate how parameter values affect the patterning of the Ficoll solution by performing parametric sweeps on the parameters. This would not have been possible with 3D simulations due to the computational expenses involved. During the sweeps, the other parameters remain at their default values as summarized in Tab. 4.1.

The maximum normal displacement  $d_n^{\max}$ , or equivalently, the acoustic pressure using the plane-wave approximation, represents the acoustic intensity  $I_{\text{ac}} \propto (d_n^{\max})^2$ . Figure 6.2 summarizes the results of

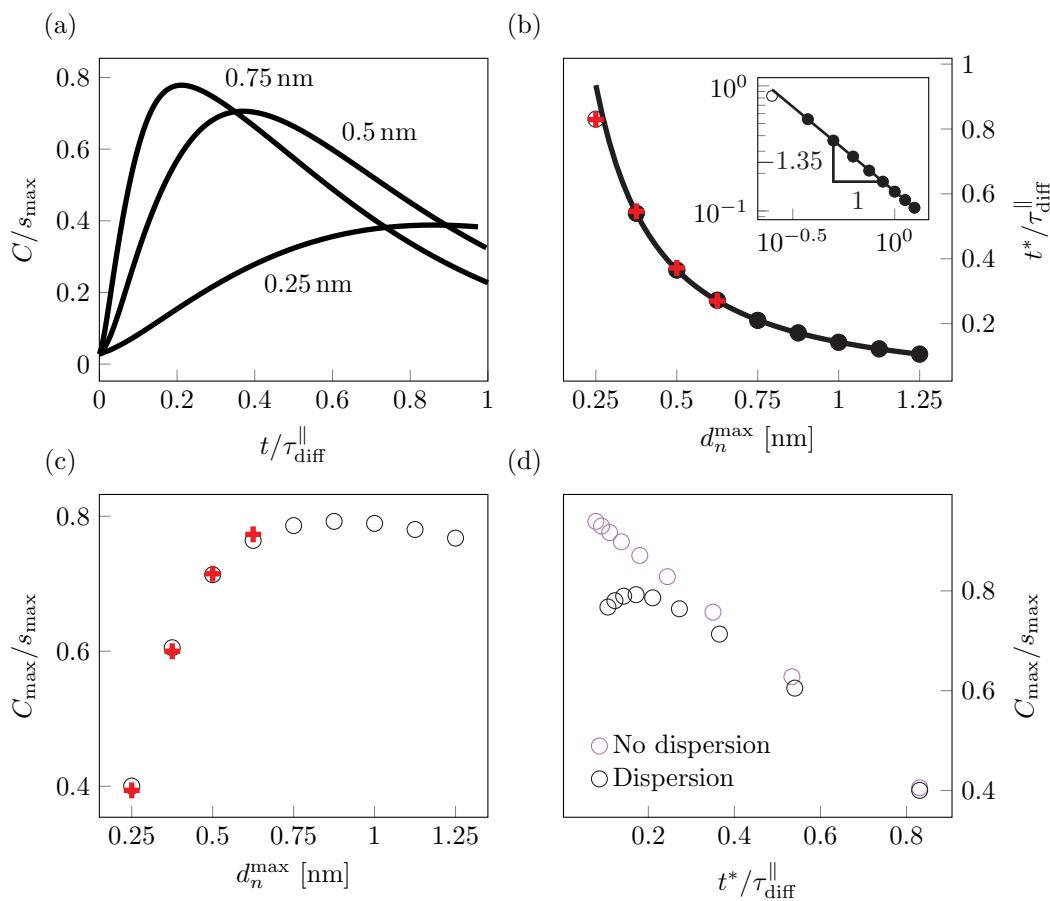


Figure 6.2: Sweep on the maximum normal displacement  $d_n^{\max}$ . Calculated by the improved 2D model with dispersion (circular, black) and the 3D model (crosses, red). (a) Contrast curves for  $d_n^{\max} = 0.25$  nm,  $0.5$  nm, and  $0.75$  nm. (b) The patterning time  $t^*$  vs.  $d_n^{\max}$ . Insert is a log-log plot. (c) The maximum contrast  $C_{\max}$  vs.  $d_n^{\max}$ . Insert is a log-log plot. Line is fitted to solid points on log scale. (d)  $C_{\max}$  vs.  $t^*$ . Violet points is calculated with the improved 2D model without dispersion.

a parameter sweep conducted on  $d_n^{\max}$ . The contrast curves corresponding to  $d_n^{\max} = 0.25$  nm, 0.5 nm, and 0.75 nm are shown in Fig. 6.2(a). The initial steepness of the curves increases with increasing  $d_n^{\max}$ , leading to shorter patterning times  $t^*$  and greater peaks  $C_{\max}$ . The life-spans also shorten with increasing  $d_n^{\max}$ , because the greater contrast peaks imply greater concentration gradients and thus greater diffusive fluxes. The time  $t^*$  is plotted vs.  $d_n^{\max}$  on the range 0.25 nm–1.25 nm in Fig. 6.2(b). From the linear tendency of the log-transformed data shown in the insert, the relationship between  $t^*$  and  $d_n^{\max}$  is clearly exponential. By fitting a linear function to the log-transformed data, we obtain the following scaling relation:  $t^* \propto (d_n^{\max})^{-1.35}$ . The negative power indicates the  $t^*$  becomes shorter with increasing  $d_n^{\max}$ . Moreover, the power being  $-1.35$  suggests a weaker dependency of  $t^*$  on  $d_n^{\max}$  than we would have expected from the equations: the acoustic force density  $\mathbf{f}_{\text{ac}}$  depends on the acoustic fields squared and thus, we would have expected the power to be  $-2$ . This non-linear scaling results from the complex interdependence of the fields. The flow velocity, driven by  $\mathbf{f}_{\text{ac}}$ , enters the advection-diffusion equation governing the concentration  $s$  through advection and dispersion. This  $s$  enters the viscosity  $\eta$  of the fluid, thus forming an indirect link between the flow velocity and itself. By eliminating dispersion from the simulations, the power becomes  $-1.65$ . By also eliminating the  $s$ -dependency of  $\eta$ , the power becomes  $-1.81$ .

The maximum concentration contrast  $C_{\max}$  is plotted against  $d_n^{\max}$  in Fig. 6.2(c) and  $t^*$  in Fig. 6.2(d). Initially,  $C_{\max}$  increases with increasing  $d_n^{\max}$ , inversely of  $t^*$  as expected if  $C_{\max}$  is determined by the competition between advection and diffusion. At intermediate values of  $d_n^{\max}$ ,  $C_{\max}$  appears to peak at 0.8 nm with a value of approximately  $0.8s_{\max}$  before decreasing at higher  $d_n^{\max}$ . This peaking and subsequent decreasing of  $C_{\max}$  was found to be a result of dispersion. Without dispersion, the data points of  $C_{\max}$  and  $t^*$  lie on a straight line (violet points) with a negative slope as expected if  $C_{\max} \propto \tau_{\text{diff}}/t^*$ . Whether this plateauing is accurately represented by the model is hard to determine. With  $\epsilon = 0.62$  and  $Pe \gtrsim 5$  at  $d_n^{\max} = 1$  nm, we are far beyond the formal limit of the model, and therefore we cannot trust it completely. Because 3D simulations are not possible to perform at this  $Pe$ , I was unable to settle this question. In hindsight, the parametric sweeps should have been performed at a lower  $\epsilon$  to have more confidence in the results.

The results of a parametric sweep conducted on the maximum initial Ficoll concentration  $s_{\max}$  is summarized in Fig. 6.3. The contrast curves for  $s_{\max} = 0.05, 0.1,$  and  $0.15$  (blue, red, green) is shown in Fig. 6.3(a). The patterning times  $t^*$  are plotted vs.  $s_{\max}$  in Fig. 6.3(b), and the maximum contrast values  $C_{\max}$  are plotted vs.  $s_{\max}$  in Fig. 6.3(c). For increasing  $s_{\max}$ ,  $t^*$  initially decreases steeply, likely due to the concentration gradient, and hence  $\mathbf{f}_{\text{ac}}$ , scaling linearly with  $s_{\max}$ . The patterning times then flattens around  $s_{\max} \approx 0.1$  before becoming longer again. Some kind of flattening is expected, because there comes a point where the higher viscosity,  $\eta \propto \exp(bs)$ , must become more important than the greater concentration gradient. The subsequent increase of  $t^*$  with increasing  $s_{\max}$  is therefore also expected. However, with  $b = 16.2$ , we would expect the viscosity to be more prominent than observed. Like  $t^*$ , the maximum contrast value  $C_{\max}$  also initially increases with  $s_{\max}$ . It maximizes around  $s_{\max} \approx 0.1$  before decreasing again, which is correlated with  $t^*$ . As pointed out earlier,  $C_{\max}$  is mostly determined by  $t^*$  relative to the diffusive time scale  $\tau_{\text{diff}}^{\parallel}$ , implying a linear relationship between  $C_{\max}$  and  $t^*$ . This

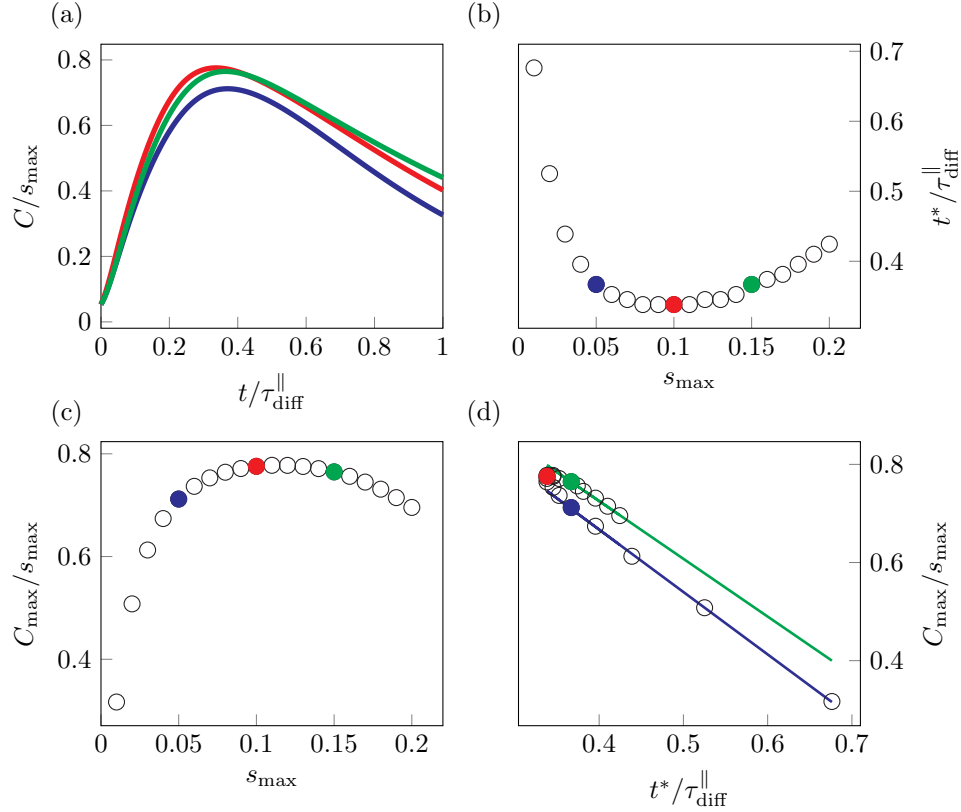


Figure 6.3: Sweep on the maximum initial Ficoll concentration  $s_{\max}$ . (a) Contrast curves for  $s_{\max} = 0.05, 0.1, \text{ and } 0.15$  (blue, red, green). The marked points in the other plots corresponds to these curves. (b) The patterning time  $t^*$  vs.  $s_{\max}$ . (c) The maximum contrast  $C_{\max}$  vs.  $s_{\max}$ . (d)  $C_{\max}$  vs.  $t^*$ . The lines show the linear relationships between  $C_{\max}$  and  $t^*$  around  $s_{\max} = 0.1$ .

is shown in Fig. 6.3(d), but, disregarding the points around  $s_{\max} = 0.1$ , one will notice that we get two lines instead of a single line. The reason for this is that the diffusivity  $D$  is lower for the data points on the green line than for those on the blue line. This can be seen from the plot of the diffusivity in Fig. 2.1. Upon rerunning the sweep for  $d_n^{\max} = 0.75$  nm, hereby increasing  $Pe$  and reducing the importance of diffusion, the data points fall onto a single line in support of the hypothesis.

Finally, the impact of the initial width  $y_0$  and the gradient width  $w_0$  have been shown in Fig. 6.4. The contrast curves for  $ky_0 = 1.8, 2.6, \text{ and } 3.7$  are shown in Fig. 6.4(a). For  $ky_0 = 3.7$ , the contrast does not change before  $t = 0.1\tau_{\text{diff}}^{\parallel}$  at least. It turns out that this is due to the initial concentration gradient not significantly overlapping with the first maximum ring of the acoustic force-shape function  $F_{\text{ac}}$ . This situation is sketched in Fig. 6.4(b), in which  $F_{\text{ac}}$  (red) is superimposed on the initial concentration profiles of width  $ky_0 = 3.6$  and two different gradient widths  $w_0$  (black and gray). Due to the concentration being constant in the region of the maximum of  $F_{\text{ac}}$  indicated by the solid vertical line, there is little interaction between  $F_{\text{ac}}$  and the concentration gradient to give a significant force. Consequently, there is a window

of time, during which there is no force on the Ficoll solution, until the gradient is sufficiently broadened by diffusion. For  $y_0 < r_{\text{ac}}^{\text{max}}$ , with  $r_{\text{ac}}^{\text{max}}$  being the radial distance to the maximum of  $F_{\text{ac}}$ , the initial gradient always intersect with the maximum at some point along the arc with radius  $r_{\text{ac}}^{\text{max}}$ . The patterning time  $t^*$  vs.  $ky_0$  for the profiles (black and gray) is shown in Fig. 6.4(c). The black vertical line indicates  $r_{\text{ac}}^{\text{max}}$ ; the black and gray dashed lines indicate this  $r_{\text{ac}}^{\text{max}}$  plus their respective  $w_0$ . The two lines are fitted to the solid data points in log-space, yielding powers of 1 (black) and 0.67 (gray). The greater  $w_0$ , the greater  $t^*$ . The main effect of increasing  $w_0$  is that  $t^*$  is increased for all  $y_0$  due to the initial gradient,  $|\nabla s_0| \sim s_{\text{max}}/w_0$ , becoming less steep. Furthermore, the fit to the solid points appears to extrapolate  $t^*$  further beyond  $r_{\text{ac}}^{\text{max}}$  for the wider gradient width  $w_0$  (gray)  $w_0$  than the narrower (black). I believe this is because the acoustic force-shape maximum overlaps with the initial gradient up to around the gray dashed line for the wider  $w_0$ , whereas it only overlaps with the gradient up to the right black dashed line for the narrow  $w_0$ . The calculated  $t^*$  from a sweep conducted on  $w_0$  is shown in Fig. 6.4(d), showing that  $t^*$  increases with  $w_0$  as expected.

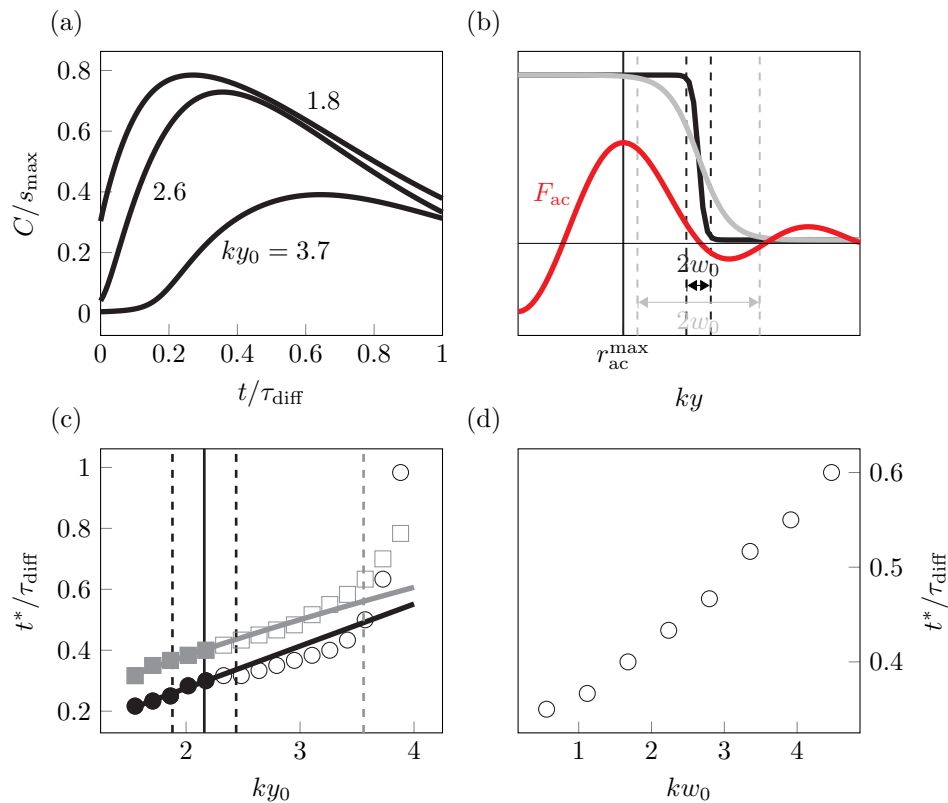


Figure 6.4: Sweeps on the initial width  $y_0$  and gradient with  $w_0$  of the initial concentration band of Ficoll. (a) The contrast curves for  $ky_0 = 1.8, 2.6,$  and  $3.7$ . (b) Sketch of interaction between the acoustic force shape-function  $F_{\text{ac}}$  (red) and the gradients of two initial concentration profiles with  $w_0 = 9 \mu\text{m}$  (black) and  $45 \mu\text{m}$  (gray). The dashed lines indicate the width  $w_0$  of the profiles. The vertical solid line indicate the point  $r_{\text{ac}}^{\max}$  of the maximum of  $F_{\text{ac}}$ . (c) The patterning time  $t^*$  vs.  $ky_0$  for the two foregoing profiles (black and gray). Lines are fitted to solid points. Black vertical line indicate  $r_{\text{ac}}^{\max}$  at which  $F_{\text{ac}}$  attains its maximum. Dashed lines indicate  $r_{\text{ac}}^{\max} \pm w_0$  for the two profiles (black and gray). (d) The times  $t^*$  plotted against  $kw_0$ .

# Chapter 7

## Experimental comparisons

Ultimately, the goal is to develop a numerical model that accurately describes the patterning of inhomogeneous fluid solutions using acoustics. Within the foregoing chapters, we have formulated a 2D model of this patterning and tested it against a 3D model with errors only amounting to a few percent. In this chapter, the 2D model undergoes its ultimate trial: it is directly compared to the experimental data.

The experimental data used for this comparison has been collected and pre-processed by our experimental collaborators at Lille University: PhD student Samir Almohamad, CR Sarah Cleve, and Professor Michaël Baudoin. For a brief description of the data and our collaborators' experimental setup, the reader is referred to Chapter 1.

Within this chapter, the first section describes the minor adjustments and additions made to the model in order to achieve the best comparison between simulation and experiment, including the determination of the initial concentration profile of Ficoll PM400. The second and final section presents a comparison and discussion of the simulation and experimental results.

### 7.1 Determining the initial concentration profile

In the experiments, the center of the acoustic vortex does not appear to fall perfectly on top of the band of Ficoll. This is evidenced by the pattern not mirroring itself across the longitudinal axis of the band (Fig 1.1(b)), parallel to the  $x$ -axis. In the simulations, instead of adjusting the vortex center directly, the initial concentration profile is translated by a constant  $y_c$  along the  $y$ -axis. This translation is implemented by the substitution  $y \rightarrow y - y_c$ . Hence, the initial concentration profile of Ficoll is described by

$$s_0 = s_{\min} + \frac{1}{4}(s_{\max} - s_{\min}) \left[ 1 + \tanh \left( \frac{(y - y_c) + y_0}{w_0/2} \right) \right] \left[ 1 + \tanh \left( \frac{y_0 - (y - y_c)}{w_0/2} \right) \right]. \quad (7.1)$$

Here,  $y_c > 0$  corresponds to moving the concentration band up relative to the vortex center and  $y_c < 0$  the opposite action. For the present comparison,  $y_c = -y_0/3$  is chosen; but, in the future, this parameter need to be determined carefully.

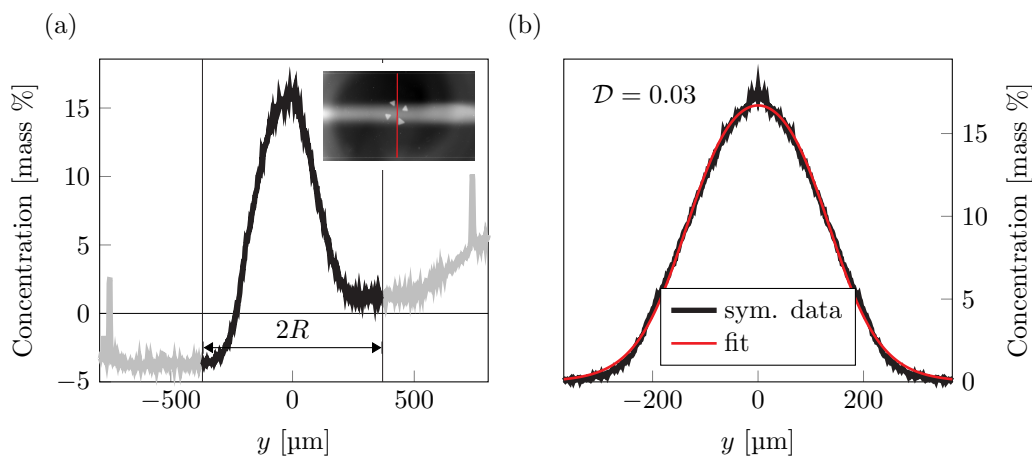


Figure 7.1: Experimental data of initial Ficoll PM400 concentration profile. Data adapted from Ref. [14]. (a) Plot of concentration data. Black data points, corresponding to the part of the profile contained within the volume of the computational domain, are used for fitting, while the grayed-out points are excluded from the analysis. Insert: Image of initial distribution of Ficoll (white) in water (dark); data is collected along the red line in the image; note that the fluid colors in this image are inverted from previous experimental images. (b) Plot of symmetrized data points (black) and fit of Eq. (4.1) (red). The discrepancy  $\mathcal{D}$  between the data points and the fit is 0.03.

To determine the parameters  $s_{\max}$ ,  $y_0$ , and  $w_0$  entering Eq. (7.1), this equation is fitted to experimental data of the initial concentration profile of Ficoll. This data is shown in Fig. 7.1(a). Negative concentration values are attributed to artifacts in the background. The data is symmetrized and subsequently fitted by minimization of the discrepancy  $\mathcal{D}$  between Eq. (7.1) and the data using MATLAB's `fminsearchbnd`. This fit and the symmetrized data is shown in Fig. 7.1(b). The resulting fitting parameters are found in Tab. 7.1, tabulating the parameter values of the simulation used for experimental comparison. This simulation required 700,000 degrees of freedom and took 1 day, 13 hours to complete.

## 7.2 Comparison of simulations and experimental data

Figure 7.3 shows the evolution of the pattern in both experiment and simulation. The time points are selected such that the patterns are compared at the same stage of their evolution relative to the patterning time. Qualitatively, we observe good agreement between simulation and experiment. This indicates that the off-axis placement of the acoustic vortex successfully reproduces the asymmetric pattern observed in experiments. Nonetheless, the gap between the acoustic center and the first arm of Ficoll appears inconsistent between simulation and experiment. In simulation, this distance is approximately  $150 \mu\text{m}$ , but, in experiments, it is closer to  $200 \mu\text{m}$ .

Furthermore, when comparing their contrast curves, as shown in Fig. 7.2, we note a lack of overlap between the curves. The initial contrast is much lower in simulations than in experiment, and the

Table 7.1: Parameter values used in simulation for experimental comparison.

<i>Acoustic parameters</i>			<i>Solute parameters</i>			<i>Geometry</i>		
Symbol	Value	Units	Symbol	Value	Units	Symbol	Value	Units
$f$	17.3	MHz	$s_{\max}$	0.189	1	$h$	20	$\mu\text{m}$
$c_g$	3500	$\text{m s}^{-1}$	$s_{\min}$	0.001	1	$R$	370	$\mu\text{m}$
$d_n^{\max}$	1.5	nm	$y_0$	135	$\mu\text{m}$	$R_1$	163	$\mu\text{m}$
$p_{\text{ac}}^{\max}$	0.57	MPa	$w_0$	196	$\mu\text{m}$	$R_2$	268	$\mu\text{m}$
$\lambda$	202	$\mu\text{m}$	$y_c$	-45	$\mu\text{m}$			

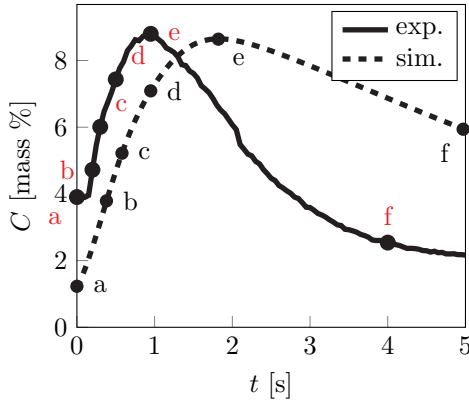


Figure 7.2: Comparison of concentration contrast of simulation (dashed) and experiment (solid). Letters correspond to the panels in Fig. 7.3. Black = simulation; red = experiment. Experimental data adapted from Ref. [14].

patterning times are significantly different, being 1.8 s and 0.95 s, respectively, indicating that the acoustic intensity used in simulations is insufficient. The inconsistency of the initial contrast value is partially explained by the aforementioned gap-difference between simulation and experiment. The maximum contrast values are nearly identical, 8.6 mass % in simulations and 8.8 mass % in experiments, the general inconsistency between the curves, however, render this inconclusive.

Another striking difference between the two curves is the diffusive decay of the pattern, which occurs much faster in experiments than in simulations. In experiments, this decay is only slightly slower than the patterning time; in simulations, it is much slower than the patterning time. Some of this is attributed to the difference in patterning time of simulations and experiments, since the immediate decay of the pattern depends on the concentration gradient at the contrast peak. However, this cannot explain all of it, and there must be another mechanism at work, which is not accounted for in simulations.

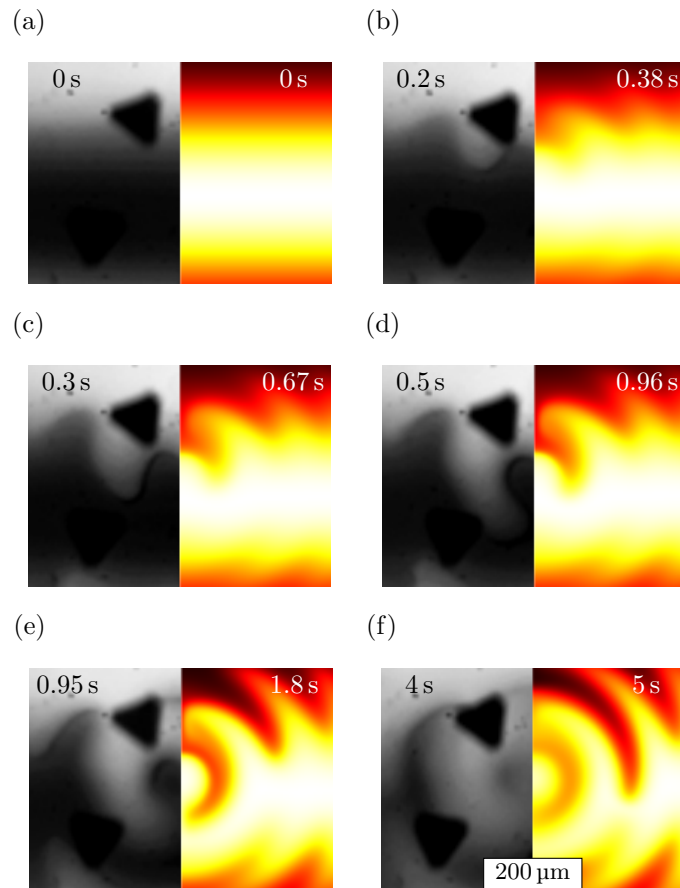


Figure 7.3: Visual comparison of pattern of simulation and experiment. Times are chosen such that they correspond to the same time relative the patterning time of experiments and simulation, except for the last panel. Experimental images adapted from Ref. [14].

## Chapter 8

# Conclusion & Outlook

In this thesis, we have theoretically investigated the acoustic-induced patterning of inhomogeneous solutions of Ficoll PM400 in a shallow microfluidic chamber using 2D models formulated with height-averaged quantities. These 2D models are formulated in the long-wavelength limit characterized by the small parameter  $\epsilon = kh \ll 1$  termed acoustic aspect ratio. Each model improved on its predecessor by incorporating additional complexity.

Under the long-wavelength assumption, the patterning is described by a 2D Hele-Shaw flow with the acoustic force density serving as driving force. By assuming a parabolic height-profile in the velocity, which is a characteristic feature of Hele-Shaw flows, height-averaged equations can be derived. At the experimental value of  $\epsilon = 0.62$ , this assumption leads to errors of approximately 2% due to the overestimation of the viscous resistance. In order to achieve the most accurate 2D description of the patterning at  $\epsilon = 0.62$ , when compared with a 3D model, we have included the lateral gradients of velocity and Taylor dispersion, while still assuming the parabolic velocity profile in the height. This height-averaged 2D model have shown remarkable agreement with the 3D model at  $\epsilon = 0.62$ , with errors amounting to only 1% when comparing their contrast curves.

The 2D models resulted in substantially shorter computation times, enabling a broader and more in-depth analysis of the patterning. When using a default set of parameter values, the 3D model required 600,000 degrees of freedom and took approximately 3 hours to finish. In contrast, the 2D models only required 40,000 degrees of freedom and completed on 5 minutes. For higher Péclet numbers, the computation times of the 2D models would be extended significantly, sometimes spanning hours or even days. These prolonged computation times stems from the requirement of using more refined meshes at higher Péclet numbers. Simulations in 3D at these Péclet numbers were not attempted. In the future, it would be beneficial to consider implementing stabilization methods to increase the robustness and computational efficiency of the simulations.

Finally, the contrast curve of the 2D model was compared with experimental data, showing qualitative agreement between simulations and data. However, significant quantitative discrepancies were observed, which require further investigations. In particular, the ‘long time’ diffusive dissolution of the pattern is

greatly underestimated in simulations, strongly suggesting the involvement of other mechanisms. This discrepancy should be investigated in future works, especially for those seeking to make more accurate experimental comparisons.

## Appendix A

# Instantaneous point-source diffusion in cylindrical box

We consider the diffusion of an instantaneous point-source in a cylindrical box. This geometry is sketched in Fig. A.1.

The instantaneous point-source is described by the following initial condition:

$$s_0 \equiv s(\mathbf{r}, t = 0) = S_0 \delta^d(\mathbf{r}), \quad (\text{A.1})$$

in which  $S_0 = \int_{\Omega} s_0 dV$  is the total amount of solute introduced at  $t = 0$ , and  $\delta^d$  denotes the  $d$ -dimensional Dirac delta function.

For  $t > 0$ , the evolution of the solute distribution follows the diffusion equation, which is given by

$$\partial_t s = D_0 \nabla^2 s, \quad (\text{A.2})$$

with  $D_0 = 1.15 \times 10^{-10} \text{ m}^2 \text{ s}^{-1}$  a constant diffusion coefficient. On the walls of the box, we have the no-flux condition:

$$(\hat{\mathbf{n}} \cdot \nabla) s = 0. \quad (\text{A.3})$$

The problem admits two characteristic lengths:  $h$  and  $R$ . The ratio of these lengths defines the aspect ratio  $\epsilon$ ,

$$\epsilon = \frac{h}{R} = 0.03 \ll 1. \quad (\text{A.4})$$

The disparity between two characteristic lengths gives rise to a long time scale  $\tau_{\text{diff}}^{(R)}$  set by radial diffusion, and a short time scale  $\tau_{\text{diff}}^{(h)}$  set by diffusion in the height. These diffusion time scales are given by

$$\tau_{\text{diff}}^{(R)} = \frac{R^2}{D_0}, \quad \tau_{\text{diff}}^{(h)} = \frac{h^2}{D_0} = \epsilon^2 \tau_{\text{diff}}^{(R)}. \quad (\text{A.5})$$

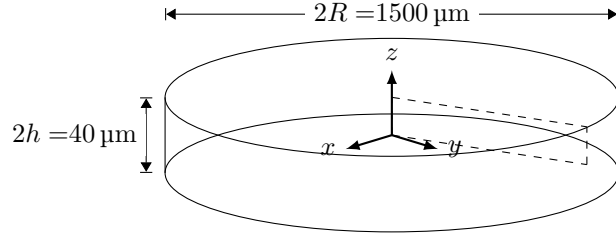


Figure A.1: Sketch of cylindrical box. The rectangular cross-section surrounded by a dashed line represents the computational domain. The aspect ratio is  $\epsilon = 0.03$ .

When simulating, we exploit the azimuthal symmetry of the problem and reduce the geometry to the 2D plane of area  $Rh$  shown by the dashed boundaries in Fig. A.1. Furthermore, instead of simulating the Dirac-delta function given in Eq. (A.1), we imagine that we wait a short period of time  $t_0 \ll \tau_{\text{diff}}^{(h)}$ , during which the initial point-source distribution develops into a normal distribution described by

$$s = S_0(4\pi D_0 t)^{-d/2} \exp\left(-\frac{r^2}{4D_0 t}\right) \quad \text{for } t > 0, \quad (\text{A.6})$$

which is the exact analytical solution of the unbounded problem [16]. In  $r = 0$ , the concentration at the initial source decays exponentially with the number of dimensions  $d$  to its power,

$$s(\mathbf{r} = \mathbf{0}, t) = S_0(4\pi D_0 t)^{-\frac{d}{2}}, \quad t > 0, \quad (\text{A.7})$$

which is characteristic of diffusion in an unbounded domain. This exponential decay is shown in Fig. A.2(a), normalized by the time  $t_0$  at which we begin observing the diffusion.

The time  $t_0$  need to be much shorter than the short diffusive time scale, so that the concentration field does not feel the outer boundaries of the cylindrical box. In principle, the development into the normal distribution occurs instantaneously, but the shorter we pick  $t_0$ , the finer mesh is required to resolve the initial distribution. We pick  $t_0 = 0.01\tau_{\text{diff}}^{(h)}$ , and the initial distribution  $s_0$  in 3D is thus described by

$$s_0 = S'_0 \exp\left(-\frac{r^2}{4D_0 t_0}\right), \quad (\text{A.8})$$

in which we redefined the initial amount of solute,

$$S'_0 \equiv S_0(4\pi D_0 t_0)^{-3/2}. \quad (\text{A.9})$$

The decay of the concentration field in  $r = 0$  for the bounded diffusion in a cylindrical box is shown in Fig. A.2(b). Initially, the diffusion exhibits the behaviour of 3D unbounded diffusion. On the diffusive time scale of the height,  $\tau_{\text{diff}}^{(h)}$ , the concentration field begins to feel the top and bottom walls on which the no-flux condition applies. Eventually it is entirely diffused in the height of the box, and the diffusion becomes entirely radial 2D diffusion. This is confirmed by plotting the analytical solutions of 2D and 3D

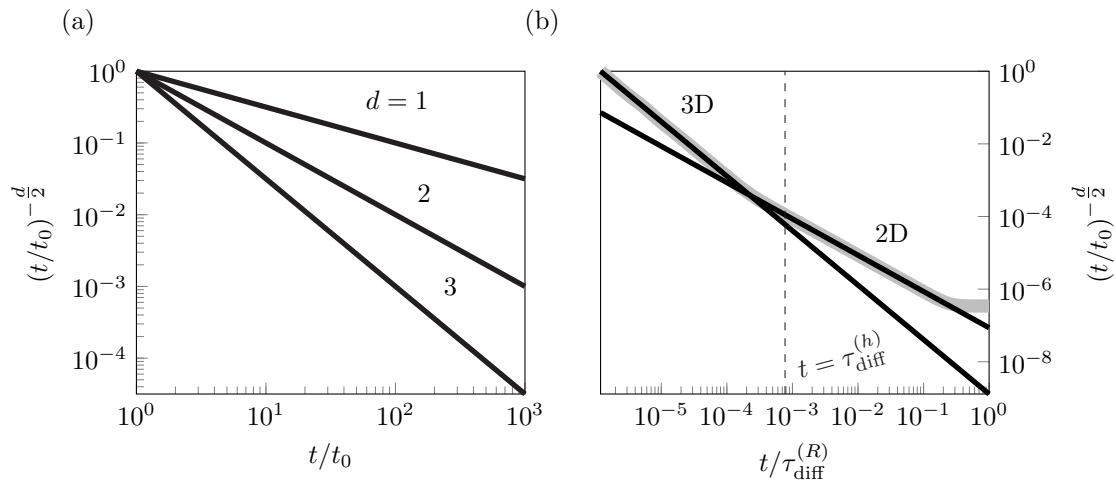


Figure A.2: Diffusion of an instantaneous point-source. (a) Analytical solution of unbounded diffusion of an instantaneous point-source, evaluated at the point of the initial source. (b) Numerical solution of bounded diffusion of an instantaneous point-source, evaluated at the point of the initial source. The solid lines of different slopes are the 2D and 3D analytical solutions of diffusion in an unbounded domain. The vertical dashed line indicates the diffusive time scale in the height,  $\tau_{\text{diff}}^{(h)}$ .

diffusion in an unbounded domain, which are shown as the solid lines in the plot.



# Appendix B

## Gravity simulation

We consider a solution of Ficoll PM400 in water in the shallow chamber shown Fig. B.1. The initial distribution of Ficoll in the chamber is described by

$$s_0 \equiv s(x, y, z, t = 0) = s_{\min} + \frac{1}{4}(s_{\max} - s_{\min}) \left[ 1 + \tanh\left(\frac{y + y_0}{w_0/2}\right) \right] \left[ 1 + \tanh\left(\frac{y_0 - y}{w_0/2}\right) \right]. \quad (\text{B.1})$$

In absence of acoustic fields, the particles of the dense Ficoll solution fall to the bottom of the chamber due to gravity-driven convection. This process is described by the following set of equations:

$$0 = \nabla \cdot \mathbf{v}, \quad (\text{B.2a})$$

$$\rho \partial_t \mathbf{v} = -\nabla p + \eta \nabla^2 \mathbf{v} + \rho_w a_1 s \mathbf{g}, \quad (\text{B.2b})$$

$$\partial_t s + (\mathbf{v} \cdot \nabla) s = \nabla \cdot (D \nabla s), \quad (\text{B.2c})$$

The non-linear advective term in the Navier–Stokes equation is neglected on account of its smallness.

Because the initial profile (B.2) is independent of  $x$  and  $L \gg y_0$ , the computational domain can be reduced to the cross-sectional plane indicated by the dashed lines in Fig. B.1.

Convection occurs at the interface between the Ficoll solution and the pure water. Evaluating the

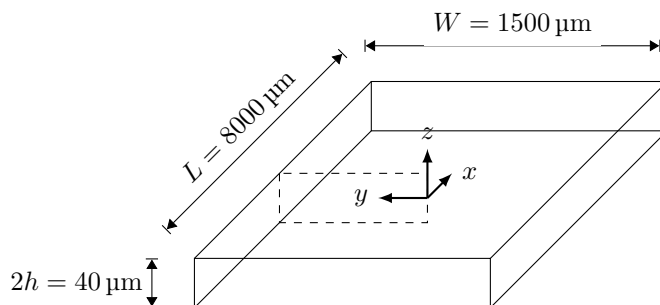


Figure B.1: Sketch of microfluidic chamber. Dashed domain indicates the computational domain.

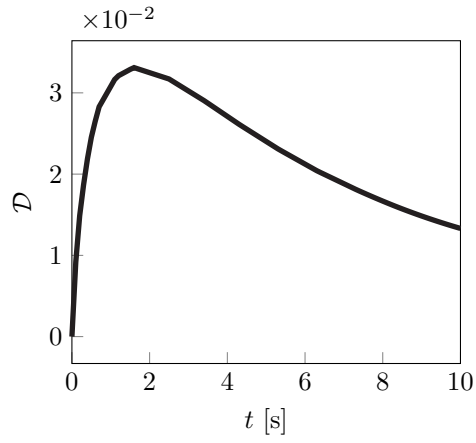


Figure B.2: The relative variation of the Ficoll concentration over the height due to gravity-driven convection.

height variation  $s - \langle s \rangle$  of the concentration relative to the height-averaged concentration  $\langle s \rangle$  at this interface in  $y = y_0$  by the normalized  $L^2$ -norm yields the plot in Fig. B.2. Here, we see that convection leads to a variation on  $\approx 3\%$ . This variation exponentially decays due to diffusion.

## Appendix C

# Acoustics and gravity

Including the acoustic force density, gravity does not play a role. The concentration contrast calculated with and without gravity is seen in Fig. C.1. The 3D simulation accounting for gravity yields the exact same concentration contrast curve as the simulation without gravity.

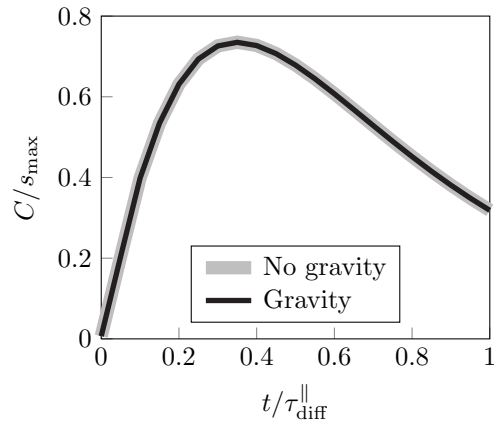


Figure C.1: Concentration contrast of 3D simulation without gravity (gray) and with gravity (black).



## Appendix D

# Influence of viscosity variation

The viscosity can be written as

$$\begin{aligned}
 \eta &= \eta_w \exp(b\langle s^{(0)} \rangle + bs^{(1)}) \\
 &= \eta_w \exp(b\langle s^{(0)} \rangle) + \eta_w \exp(b\langle s^{(0)} \rangle) [\exp(bs^{(1)}) - 1] \\
 &\approx \eta_w \exp(b\langle s^{(0)} \rangle) (1 + bs^{(1)}).
 \end{aligned} \tag{D.1}$$

This expansion is justified by  $s^{(1)} \sim \epsilon/15$  and  $b/15 \sim 1$ , so  $b_1 s^{(1)} \sim \epsilon$ , and the argument in the exponential function due to  $s^{(1)}$  is small. The height-dependency of viscosity leads to the following correction in  $\mathbf{f}_{\text{visc}}$ ,

$$\begin{aligned}
 \mathbf{f}_{\text{visc}} &= -\frac{12\eta^{(0)}}{(2h)^2} \langle \mathbf{v}^{(0)} \rangle - \langle \partial_z(\eta^{(1)} \partial_z \zeta) \rangle \langle \mathbf{v}^{(0)} \rangle \\
 &= -\frac{12\eta^{(0)}}{(2h)^2} \langle \mathbf{v}^{(0)} \rangle - \eta^{(0)} \langle \partial_z(bs^{(1)} \partial_z \zeta) \rangle \langle \mathbf{v}^{(0)} \rangle \\
 &= -\frac{12\eta^{(0)}}{(2h)^2} \left(1 + bs^{(1)}(h)\right) \langle \mathbf{v}^{(0)} \rangle,
 \end{aligned} \tag{D.2}$$

This additional term appears from the divergence of viscous stresses. The variation of the Ficoll concentration is given by

$$s^{(1)}(h) = \frac{h^2}{15D^{(0)}} (\langle \mathbf{v}^{(0)} \rangle \cdot \nabla) \langle s^{(0)} \rangle. \tag{D.3}$$

The result of including this is shown in Fig. D.1. Including this viscosity variation slightly underestimates the contrast curve, although it is hardly noticeable. For better agreement, we should take into account that the resistance is not exactly that of Hele-Shaw. It is smaller by the assumed resistance by about 2%. Therefore, this model of the variation of viscosity over the height can still be better, but other errors make it worse than a slightly simpler model.

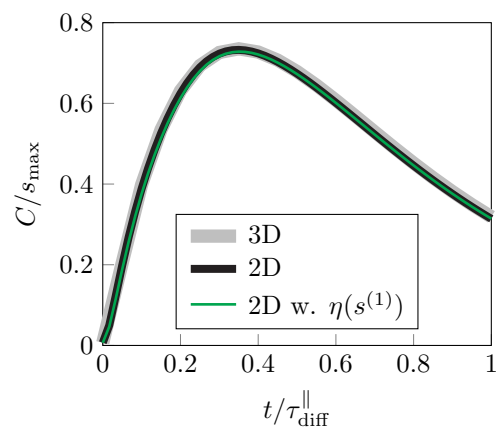


Figure D.1: The influence of viscous variation over height. Contrast of 3D model, improved 2D model, and improved 2D model with viscosity height-variation.

# Bibliography

- [1] J. Rufo, F. Cai, J. Friend, M. Wiklund, and T. Huang, *Acoustofluidics for biomedical applications*. Nature Reviews Methods Primers **2**, 30 (2022).
- [2] L. V. King, *On the acoustic radiation pressure on spheres*. Proceedings of the Royal Society of London. Series A - Mathematical and Physical Sciences **147**(861), 212–240 (1934).
- [3] K. Yosioka, *Acoustic radiation pressure on a compressible sphere*. Acustica **5**, 167–173 (1955).
- [4] L. Gor'kov, *On the forces acting on a small particle in an acoustical field in an ideal fluid*. Sov. Phys.-Doklady **6**, 773–775 (1962).
- [5] H. Bruus, *Acoustofluidics 7: The acoustic radiation force on small particles*. Lab Chip **12**, 1014–1021 (2012).
- [6] A. Lenshof, C. Magnusson, and T. Laurell, *Acoustofluidics 8: Applications of acoustophoresis in continuous flow microsystems*. Lab Chip **12**, 1210–1223 (2012).
- [7] M. Baudoin, J.-L. Thomas, R. Sahely, J.-C. Gerbedoen, Z. Gong, A. Sivery, O. Matar, N. Smagin, P. Favreau, and A. Vlandas, *Spatially selective manipulation of cells with single-beam acoustical tweezers*. Nature Communications **11**, 4244 (2020).
- [8] H. Bruus, *Acoustofluidics 10: Scaling laws in acoustophoresis*. Lab Chip **12**, 1578–1586 (2012).
- [9] J. F. Spengler, W. T. Coakley, and K. T. Christensen, *Microstreaming effects on particle concentration in an ultrasonic standing wave*. AIChE Journal **49**(11), 2773–2782 (2003).
- [10] L. Rayleigh, *I. on the circulation of air observed in kundt's tubes, and on some allied acoustical problems*. Philosophical Transactions of the Royal Society of London **175**, 1–21 (1884).
- [11] S. Deshmukh, Z. Brzozka, T. Laurell, and P. Augustsson, *Acoustic radiation forces at liquid interfaces impact the performance of acoustophoresis*. Lab Chip **14**, 3394–3400 (2014).
- [12] P. Augustsson, J. Karlsen, H.-W. Su, H. Bruus, and J. Voldman, *Iso-acoustic focusing of cells for size-insensitive acousto-mechanical phenotyping*. Nature Communications **7** (2016), this work is licensed under a Creative Commons Attribution 4.0 International License.

- [13] J. T. Karlsen, P. Augustsson, and H. Bruus, *Acoustic force density acting on inhomogeneous fluids in acoustic fields*. Phys. Rev. Lett. **117**, 114504 (2016).
- [14] S. Almohamad, S. Cleve, U. Ghosh, C. Ravinder, G. K. Modler, H. Bruus, and M. Baudoin, *Active manipulation of inhomogeneous miscible fluid interfaces using acoustical tweezers*. Forum Acusticum (2023).
- [15] J. T. Karlsen and H. Bruus, *Acoustic tweezing and patterning of concentration fields in microfluidics*. Phys. Rev. Appl. **7**, 034017 (2017).
- [16] H. Bruus, *Theoretical microfluidics* (Oxford University Press, Oxford) (2007).
- [17] L. Landau and E. Lifshitz, *Fluid Mechanics: Volume 6*. vb. 6 (Elsevier Science) (2013).
- [18] B. Lautrup, *Physics of Continuous Matter, Second Edition: Exotic and Everyday Phenomena in the Macroscopic World* (Taylor & Francis) (2011).
- [19] J. Happel and H. Brenner, *Low Reynolds number hydrodynamics: with special applications to particulate media*. Mechanics of Fluids and Transport Processes (Springer Netherlands) (1983).
- [20] W. Qiu, J. T. Karlsen, H. Bruus, and P. Augustsson, *Experimental characterization of acoustic streaming in gradients of density and compressibility*. Phys. Rev. Appl. **11**, 024018 (2019).
- [21] H. Bruus, *Numerical studies in physics*. DTU Lecture Notes (2022).
- [22] *COMSOL Multiphysics: About Numerical Stabilization in COMSOL*. [https://doc.comsol.com/5.5/doc/com.comsol.help.comsol/comsol\\_ref\\_modeling.10.75.html](https://doc.comsol.com/5.5/doc/com.comsol.help.comsol/comsol_ref_modeling.10.75.html), accessed: 2023-07-11.
- [23] G. I. Taylor, *Dispersion of soluble matter in solvent flowing slowly through a tube*. Proceedings of the Royal Society of London. Series A. Mathematical and Physical Sciences **219**(1137), 186–203 (1953).
- [24] R. Aris and G. I. Taylor, *On the dispersion of a solute in a fluid flowing through a tube*. Proceedings of the Royal Society of London. Series A. Mathematical and Physical Sciences **235**(1200), 67–77 (1956).
- [25] H. A. Stone and H. Brenner, *Dispersion in flows with streamwise variations of mean velocity: radial flow*. Industrial & Engineering Chemistry Research **38**(3), 851–854 (1999).